npj Materials Degradation

https://doi.org/10.1038/s41529-026-00777-w

Article in Press

Mechanical degradation of carbon fiber reinforced polymer composites under coupled multi-factor aging in a simulated polar environment

Received: 5 January 2026

Accepted: 17 March 2026

Cite this article as: Zhang, M., Li, W., Yin, W. *et al.* Mechanical degradation of carbon fiber reinforced polymer composites under coupled multi-factor aging in a simulated polar environment. *npj Mater Degrad* (2026). https://doi.org/10.1038/s41529-026-00777-w

Meiqi Zhang, Wei Li, Wenchang Yin, Wenhao Wan, Jiankai Li, Hongfei Liu, Cheng Man & Zhongyu Cui

Degradation of Carbon Fiber Reinforced Polymer Composites under Coupled Multi-Factor Aging in a Simulated Polar Environment

Meiqi Zhang[a, 1#], Wei Li[a, 1#], Wenchang Yin[b], Wenhao Wan[c], Jiankai Li[a], Hongfei Liu[a], Cheng Man[a] *, Zhongyu Cui[a] *

a School of Materials Science and Engineering, Ocean University of China, Qingdao 266100, China

b Unit 92228 of the People's Liberation Army, Beijing 100072, China

c NCS Testing Technology Co., Ltd., Beijing 100081, China

Abstract: Carbon fiber-reinforced polymer (CFRP) composites are pivotal to equipment in Polar Regions, yet their long-term durability in this low-temperature marine environment is severely compromised by the synergistic degradation of coupled environmental factors. Traditional single-factor aging studies cannot replicate this complex scenario, leaving a critical gap in service life prediction. An accelerated aging protocol incorporating simultaneous hygrothermal, freeze-thaw, sub-zero freezing, and UV exposure was established to systematically investigate the degradation of T700 and T800 CFRP composite materials under simulated polar environments. Results reveal that failure is fundamentally dominated by the interface variation since matrix-relevant flexural and shear strengths decline drastically (up to 45%), whereas fiber-dominated Izod impact strength remains nearly intact. A synergistic degradation sequence is proposed: the process commences with interfacial stress induced by hygrothermal swelling, followed by damage propagation during freeze-thaw cycles, stress accumulation (locking) during sub-zero freezing, and is accelerated by UV radiation, which generates defects that facilitate moisture ingress. This work provides a scientific basis for material selection, durability prediction, and the design of robust marine composite structures.

Corresponding authors, Email address: mancheng@ouc.edu.cn (C. Man); cuizhongyu@ouc.edu.cn (Z. Cui)

Key words: Carbon fiber reinforced polymer; Polar environments; Multiple environmental factors; Mechanical test; Degradation mechanism

Introduction

Carbon fiber reinforced polymer (CFRP) composites, particularly high-performance grades such as T700 and T800, have become essential materials in modern engineering [1-3]. They are widely employed in critical applications including the offshore wind turbine blades [4-6], aircrafts, and deep-sea substructures [7-10]. However, the low-temperature marine environment results in severe and complex degradation mechanisms of these composites [11-13]. This challenge is further amplified in Polar and near-Polar regions, where structures are subjected to even more extreme and sustained sub-zero temperature, prolonged seasonal ice exposure, and highly dynamic freezing-thawing conditions. It has been found that cyclic moisture absorption and desorption compromise the fiber–matrix interfacial bonding [14-17], while freezing–thawing cycles induce internal microcracking due to the pressure exerted by ice crystallization [18-22]. Prolonged exposure to subzero temperatures often embrittles the resin matrix, and ultraviolet (UV) radiation from sunlight promotes polymer chain scission [23-25]. These factors do not act in isolation in the real service environment. Instead, their synergistic interactions accelerate material aging to an extent that significantly exceeds the cumulative impact of individual effects. Consequently, the structural integrity and service life of CFRP components are substantially jeopardized [26,27].

Traditional single-factor aging tests, such as static hygrothermal exposure [28-30], UV exposure, and isolated freezing-thawing cyclic exposure [31,32], fail to accurately replicate the synergistic stress conditions encountered in actual low-temperature marine environments. Consequently, predictions of CFRP performance degradation based on such methods are often inadequate. Prior research has investigated the degradation behavior of CFRP under individual marine-related environments [33-35]. For example, the tribological response of T300-based composites at extreme temperatures has been reported, and the results suggested that the fiber had a stronger ability to increase friction than resin [36]. The interfacial degradation of epoxy-matrix composites in hygrothermal conditions is also investigated [37,38]. Results indicated that incorporating an appropriate amount of carbon

nanofibers into the epoxy resin could potentially enhance the long-term durability of such composites in hygrothermal environments [39]. Furthermore, studies have shown that the fiber–matrix interface degraded more significantly in unsaturated polyester-flax (UP-Flax) composites under similar hygrothermal exposure [40]. However, systematic studies on the coupled effects in real Polar service environment are still scarce. This gap is especially evident for high-strength T700 and T800 CFRPs simultaneously subjected to moisture exposure, freezing-thawing cycles, low-temperature embrittlement, and UV radiation. Furthermore, the establishment of standardized multi-factor accelerated aging protocols, which are essential for simulating low-temperature marine conditions, is still lacking. The absence of such tailored methodologies consequently hinders a reliable evaluation of the long-term durability of these materials.

To addressing this research gap, a multi-factor coupled accelerated aging test, specifically for T700 and T800 CFRPs, is developed in the present work. Based on an equivalent environmental acceleration spectrum derived from authentic low-temperature marine service conditions, the proposed methodology integrates sequential hygroscopic exposure, cyclic freezing-thawing, sustained low-temperature freezing, and UV irradiation. Such integration enables replication of long-term natural aging within a compressed timeframe. After the aging test, the mechanical property characterization including tensile [41,42], flexural [43,44], and interfacial shear strengths [45,46] are conducted. Through this integrated approach, the synergistic aging mechanisms induced by combined low-temperature marine environments could be unraveled.

Results

Tensile test analysis

Fig. 4 shows the macro fracture morphologies of T700-CFRP and T800-CFRP following multi-factor coupled accelerated aging tests for different cycles. The tensile failure modes of the two composites exhibit distinct characteristics. In T700-CFRP specimens, fracture is accompanied by noticeable matrix cracking and localized fiber fragmentation, resulting in a dispersed fiber-splitting morphology. This failure pattern features an irregular fracture surface with extensive

matrix damage. In contrast, the T800-CFRP composite shows a comparatively smooth fracture surface, devoid of fiber scattering or splitting, marked by fiber pull-out, which indicates a predominantly brittle failure mechanism. With prolonging aging cycles, the tensile failure intensifies and the structural integrity of the specimens deteriorates progressively. Failure initiates from external fiber and matrix fractures, then propagates inward, leading to increasingly severe internal delamination.

The tensile stress-strain responses of T700-CFRP and T800-CFRP composites after different aging cycles are presented in Fig. 5(a ~ d), with the corresponding tensile strength data summarizing in Table 1. As depicted in the stress-strain curves, all specimens exhibit an initial linear elastic region followed by a short nonlinear hardening stage before abrupt fracture. With increasing aging cycles, the strain at failure gradually decreases, and the nonlinear deformation segment shortens, indicating that multi-factor coupled aging induces progressive embrittlement of the composites. Correspondingly, the tensile modulus values were also analyzed but did not show obvious or consistent variation with increasing aging cycles. This lack of clear trend is attributed to the competing effects of matrix embrittlement, which tends to increase stiffness, interfacial debonding, microcracking, and reduce modulus. Under the combined hygrothermal, freezing-thawing, and UV aging conditions, these two mechanisms offset each other, resulting in no significant regular evolution in tensile modulus. The tensile strength retention rates of the two composite materials as a function of aging cycles are shown in Fig. 5(e ~ f). A clear degradation trend is observed for both materials, yet a stark contrast in durability is evident: T700-CFRP undergoes substantial strength reductions of 13.8% and 14.7%, markedly exceeding the 11.6% and 6.8% decreases in T800-CFRP. The superior property of T800-CFRP is attributed to its intrinsically tighter weave structure and the higher structural stability of T800 fibers, which provide better resistance to environmental degradation and more effective load transfer between fiber and matrix under coupled hygrothermal and radiative aging.

DIC analysis of the Y-direction strain evolution during tensile test (Fig. 6) reveals the failure initiation and propagation processes. A significant strain concentration first nucleates at intrinsic

weak points within the gauge section, indicating localized stress intensification. Following initial fiber breakage, the Y-direction strain distribution becomes highly heterogeneous. With continued loading, strain localizes progressively at these damage sites, further intensifying the stress concentration until critical crack propagation initiates at one of these locations, leading to final fracture. This consistent damage initiation and propagation behavior across all aging conditions confirms that the measured tensile strength degradation trends accurately reflect the material's intrinsic response to multi-factor coupled aging.

Compression test analysis

Fig. 7 presents the fracture morphologies of T700-CFRP and T800-CFRP compression specimens after multi-factor coupled accelerated aging. All specimens exhibit a dominant splitting fracture mode, with occasional oblique fracture, and failure consistently initiates within the working zone near the reinforcement patches. With increasing aging cycles, macroscopic observations reveal that crack initiation occurs at the outer layer and propagates inward, resulting in increasingly severe macroscopic damage. The consistent splitting fracture behavior under compression confirms the typical failure mechanism of carbon fiber-reinforced composites under longitudinal compression, and the aggravated damage with aging cycles indirectly demonstrates that the multi-factor coupled environment has degraded the interfacial bond strength between the resin matrix and fibers.

Analysis of the compression performance (Fig. 8, Table 2) reveals a continuous degradation in strength for both T700-CFRP and T800-CFRP with prolonged aging. The stress-strain curves in Fig. 8 exhibit significant nonlinearity prior to final failure, which is attributed to progressive internal material damage induced by multi-factor coupled aging rather than fixture compliance, specimen instability, or measurement artefacts. Specifically, with the extension of aging cycles, matrix cracking, interfacial debonding, and slight delamination are initiated and propagated within the composites. Under compressive loading, these internal defects lead to localized stress redistribution and gradual damage accumulation, which manifests as nonlinearity in the stress-strain response.

The evolution of their compressive strength retention rate, however, underscores a key difference in durability (Fig. 8e~f). T700-CFRP undergoes a two-stage degradation process, characterized by an initial slow degradation stage followed by a subsequent rapid degradation stage. In contrast, T800-CFRP exhibits a slight decrease in the compressive strength in comparison with T700-CFRP after the aging test, which is consistent with its superior durability observed in tensile tests, presumably due to its intrinsically tighter weave structure that mitigates internal damage accumulation.

Bending test analysis

Fig. 9 shows the fracture morphologies of T700-CFRP and T800-CFRP flexural specimens after multi-factor coupled accelerated aging. Both materials exhibit obvious indentations at the compressive loading points, accompanied by significant through-thickness deformation and dominant interlaminar tearing. The observed interlaminar tearing represents the typical failure mode for carbon fiber–reinforced composites under three-point bending, confirming that the tests effectively characterize the intended flexural properties. The multi-factor coupled aging environment significantly weakens the fiber/matrix interfacial bond strength, and the macroscopic flexural failure becomes much severe with the increasing aging cycles.

The flexural response of T700-CFRP and T800-CFRP composites to progressive aging, detailed in Fig. 10(a~d) (load-deflection curves) and Table 3 (strength data), reveals a continuous decline in strength for both materials. All specimens exhibit an initial linear elastic region followed by a short nonlinear segment before abrupt failure. With increasing aging cycles, the deflection at failure gradually decreases, and the nonlinear deformation segment shortens, indicating that multi-factor coupled aging induces progressive embrittlement and reduces the toughness of the composites. However, their degradation profiles, as tracked by the retention rate in Fig. 10(e~f), follow divergent patterns. T700-CFRP exhibits a two-phase degradation: an initial rapid decline followed by a slight decrease after 6 cycles. In contrast, T800-CFRP demonstrates a more uniform rate of strength reduction. Quantitatively, under the aggressive multi-factor aging of Scheme A, T700-CFRP suffers the most severe decay, with its strength plummeting from 854.3 MPa to 498.3

MPa (58.3% retention), while T800-CFRP shows superior resistance, decreasing from 805 MPa to 712.3 MPa with a reduction of 11.5%.

Izod impact test analysis

The Izod impact fracture morphologies of T700-CFRP and T800-CFRP composites presented in Fig. 11 demonstrate distinctly different failure mechanisms. T700-CFRP exhibits a typical failure mode characterized by extensive fiber breakage, interlaminar cracking, and delamination, accompanied by the formation of obvious hinge structures, indicating a relatively tough failure process. In contrast, T800-CFRP presents a dominant brittle fracture mode with limited fiber pull-out, reflecting its higher structural integrity and stronger interfacial bonding. It is noteworthy that the macroscopic damage under Scheme A is more significant than that under Scheme B. This difference is mainly attributed to the hygrothermal component in the multi-factor coupled environment, which preferentially degrades the moisture-sensitive resin matrix and weakens the fiber–matrix interfacial bonding. Given that carbon fibers are inherently immune to moisture, the degraded Izod impact resistance observed in this study, especially the more severe failure under Scheme A, can be directly ascribed to the deterioration of the matrix and interfacial regions.

The Izod impact test data for T700-CFRP and T800-CFRP composites across various aging cycles are summarized in Table 4. The results indicate that the multi-factor coupling aging induces negligible changes in the Izod impact strength of T700-CFRP and only marginal variations in T800-CFRP. This robustness can be attributed to the dominant role of carbon fibers, which are inherently resistant to environmental degradation and maintain their structural integrity even after 12 aging cycles. Consequently, the observed minor fluctuations in Izod impact strength likely stem from the aging of the resin matrix and inherent specimen variability, confining the overall performance to a limited range.

Interlaminar shear test analysis

The macroscopic shear fracture morphologies of T700-CFRP and T800-CFRP composites are presented in Fig. 12. Obvious plastic deformation can be observed in the aged specimens, which

is closely related to the significant degradation of fiber/matrix interfacial strength caused by the multi-factor coupled environmental aging. With increasing aging cycles, the deformation is further aggravated accompanied by the formation of microcracks, demonstrating the significant deterioration induced by environmental exposure. A direct comparison indicates that T700-CFRP shows more severe shear deformation, while T800-CFRP exhibits no obvious interlaminar cracking. This morphological difference further verifies that T800-CFRP presents better environmental aging resistance compared with T700-CFRP.

Shear test data (Table 5) and the evolution of interlaminar shear strength (ILSS) retention rate (Fig. 13) reveal a marked contrast in the environmental durability between the two composite materials under multi-factor aging. The ILSS of T700-CFRP degrades rapidly, exhibiting a pronounced drop before the 6th cycle, which then slows down. In contrast, T800-CFRP maintains relatively stable strength retention. Quantitatively, under Scheme A, the ILSS of T700-CFRP decreases from 43.0 MPa to 23.7 MPa, a 45% reduction, with an overall degradation range of 40-45%. The T800-CFRP composite, however, demonstrated superior stability, with a total strength decline of only 21-25%, underscoring its significantly higher resistance to environmental aging.

Water absorption analysis

Fig. 14 shows the water absorption rates of T700-CFRP and T800-CFRP composites after six aging cycles under two distinct protocols. Both composites initially exhibit rapid water uptake, with higher rates under the high-temperature conditions of Protocol A. However, the multi-factor aging test was characterized by notable mass fluctuations. This is attributed to the physical degradation—specifically, resin matrix fracture and surface delamination induced by the coupled environmental stresses, leading to mass loss that confounds the accurate measurement of water absorption. Consequently, traditional gravimetric analysis under such multi-factor conditions fails to reliably characterize the intrinsic moisture absorption behavior of the composites.

Changes in chemical structure and morphology of the CFRPs after aging test

Fig. 15 shows the Raman spectroscopy of the T800-CFRP surface after multi-factor coupled

environmental aging, which reveals the structural evolution of the composite. The spectra are characterized by two primary bands: the D band (1330-1350 cm^{-1}), associated with disordered carbon structures and defects, and the G band (1580-1600 cm^{-1}), corresponding to the in-plane vibration of sp^2-hybridized carbon in the ordered graphite lattice. Analysis shows that the I_D/I_G ratio increases to 0.99 in all the aged specimens. This increase indicates that both aging protocols introduce surface defects and structural disorder into the carbon fibers, directly evidencing the degradation at the molecular level.

Fig. 16 shows the microscopic morphologies of the CFRP surface after aging test. The results reveals that both multi-factor aging protocols severely degrade the composite surfaces, manifesting as resin matrix cracking and fragmentation, fiber debonding, and surface notch formation. The tensile fracture morphologies shown in Fig. 17 further confirm the degradation induced by environmental aging. Compared with the unaged sample, the aged specimen exhibits distinct matrix cracking, fiber-matrix debonding, and localized brittle fracture characteristics, indicating increased embrittlement of the composite after exposure to the multi-factor coupled environment. This phenomenon is consistent with the reduced tensile strength after aging, as presented in Fig. 5(e, f), demonstrating the significant deterioration of the composite under harsh environmental conditions.

Based on the integrated spectroscopic and morphological analysis, a synergistic damage sequence is proposed: hygrothermal stresses from moisture uptake initially induce interfacial stress concentrations between the fiber and resin. Subsequent freezing–thawing cycles exacerbate this damage through volumetric expansion, while prolonged low-temperature exposure further embrittles the carbon fibers. Ultimately, UV radiation accelerates surface embrittlement and promotes powdering. This cascading degradation pathway culminates in localized fiber fracture and composite failure under mechanical loading, where stress concentrations at the compromised interfaces lead to premature brittle fracture, as evidenced in the fracture morphology. Collectively, these findings demonstrate that environmental aging in the simulated Polar environment initiates at molecular and interfacial scales and progressively propagates to govern macroscopic mechanical

degradation—particularly in bending and shear modes-in high-performance CFRPs.

Reasons for the property difference between T700 and T800 CFRPs in the simulated Polar environment

Based on the experimental findings, it can be found that multi-factor coupled aging selectively degrades composite performance by preferentially attacking the fiber–matrix interface. Fig.18 compares the strength retention rate of the two CFRPs after different mechanical tests. The results reveal that T700-CFRP composites undergo more pronounced degradation than T800-CFRP counterparts. After aging, T700-CFRP exhibits particularly severe reductions in flexural and interlaminar shear strength, with retention rates ranging from 54.9% to 61.7% and from 55.1% to 60.6%, respectively. In contrast, T800-CFRP demonstrates superior retention, with flexural strength maintained at 84.3%–88.5% and interlaminar shear strength at 74.7%-79.3%.

Both tensile and compressive properties also decline under aging Scheme A, though to different degrees. Under multi-factor aging Scheme A, the tensile strength of T700-CFRP decreases by 15.8%, while T800-CFRP exhibits a maximum reduction of 11.6%. Compressive strength is more significantly affected, with T700-CFRP declining by 28.9% and T800-CFRP by 9.4%. Notably, Izod impact performance remains largely unchanged across the aging protocols.

These observations indicate that the dominant damage mechanism under multi-factor coupled aging is the weakening of fiber–matrix and fiber–fiber interfacial bonding, with minimal direct fiber damage. Consequently, the properties strongly dependent on interfacial integrity undergo significant deterioration, such as flexural and interlaminar shear strength, while tensile and compressive properties, which rely more on fiber load-bearing capacity, exhibit more moderate declines.

The superior aging resistance of T800-CFRP composites can be attributed to their distinct microstructure, characterized by a higher matrix modulus, lower free volume, and greater crosslink density. This structure forms an effective barrier against water diffusion and storage. Furthermore, fewer micro-defects and stronger interfacial bonding restrict potential pathways for moisture ingress. The resulting lower equilibrium moisture uptake in T800-CFRP composites thus

underpins their attenuated performance degradation and overall reduced sensitivity to environmental aging.

Effect of the environment characteristics on the failure mechanism of the CFRPs in the simulated Polar environment with multi-factor coupling effect

The synergistic degradation of carbon fiber composites in the simulated Polar low-temperature marine environments arises from the coupled action of four primary factors: hygrothermal, freezing-thawing, sub-zero freezing, and ultraviolet irradiation, which are the typical environmental factors suffered in Polar Regions.

Fig. 19 shows the schematic diagram of the degradation mechanism of the CFRP material in this environment. Under hygrothermal conditions, the resin matrix absorbs moisture and sweizodlls accordingly. The resulting differential expansion between the resin and the carbon fibers, due to their distinct coefficients of hygroscopic and thermal expansion, generates significant internal stress at the interface. This stress is further concentrated at inherent micro-defects, such as microcracks and voids, facilitating water ingress. When these interfacial stresses exceed the bond strength, debonding and interlaminar cracking initiate.

Subsequent freezing-thawing cycles exacerbate this damage (Fig. 19b). The phase change of imbibed water to ice within the resin and defects induces expansive stresses, while low temperature embrittles the matrix. The cyclic process of ice formation (stress) and melting (relaxation) subjects the material to a fatigue regime, progressively propagating microcracks and degrading the fiber-matrix interface.

In the following sub-zero frozen environment, the stored water transforms into higher-strength ice. This imposes a sustained internal load on the already embrittled composite, akin to a static fatigue state. This leads to further interface debonding, matrix cracking, and a marked increase in defect volume and density.

Finally, the UV irradiation attacks the moisture-conditioned resin, causing chain scission and polymer backbone degradation. This surface deterioration produces microcracks and increases surface roughness, which enhances water absorption capacity in subsequent hygrothermal

exposures and accelerates the degradation cycle.

In summary, the multi-factor coupling accelerates the composite failure through a sequential mechanism: hygrothermal swelling initiates interfacial stresses, freezing-thawing cycling propagates damage via phase-change fatigue, sub-zero freezing locks in high stresses with strong ice, and UV radiation creates surface defects that facilitate further moisture ingress. This synergistic sequence results in progressively severe performance degradation with extended aging. In the real service environment, these factors may act in sequence or simultaneously, resulting in the degradation of the CFRP materials in Polar environment.

Discussion

This manuscript investigates the aging behavior of T700 and T800 CFRPs materials in the simulated Polar environment using the mechanical test and surface observation. The main conclusions are listed as follows:

(1) Multi-factor aging predominantly compromises the bonding performance of the fiber–matrix interface, leading to marked reductions in bending and shear properties, whereas only marginal declines are observed in tensile and compressive strength.

(2) Owing to their superior microstructural characteristics, T800-CFRP composites exhibit greater resistance to moisture ingress. This, in turn, attenuates the deleterious effects of synergistic moisture–thermal–mechanical coupling on the fiber–matrix interface during accelerated aging.

(3) CFRP degradation in polar environments proceeds via a definable synergistic sequence: hygrothermal stress initiates interfacial damage, freeze-thaw cycles propagate cracks, persistent freezing locks in ice-induced stress, and UV radiation produces defects which in turn facilitate moisture ingress, collectively leading to accelerated failure.

Methods

Materials

In this study, The composites used in this study consisted of T700-CFRP and T800-CFRP fabricated by T700 and T800 carbon fibers as well as the vinyl ester resin. The composites were

directly purchased from Luoyang Institute of Shipping Materials in China. Firstly, the selected T700-CFRP and T800-CFRP specimens were carefully inspected by naked-eye visual observation to ensure no macroscale surface defects were present. Then, the raw materials were cut into the required dimensions using a water jet cutting machine to ensure dimensional accuracy and minimize surface damage. The specimen dimensions and tolerances were strictly controlled in accordance with the relevant national standards. After cutting, the specimen edges were polished with sandpaper to remove burrs and sharp edges before aging conditioning and subsequent testing.

Fig. 1 shows the schematic diagrams of the sample dimensions used for tensile test (Fig. 1a), compression test (Fig. 1b), bending test (Fig. 1c), Izod impact test (Fig. 1d), and shear test (Fig. 1e), according to the standards of GB/T 1447-2005 [47], GB/T 1448-2005 [48], GB/T 33621-2017 [49], GB/T 1843-2008 [50], and GB/T 30969-2014 [51], respectively. The samples were prepared based on these requirements and the detailed procedures are given in section 2.3.

For compression tests, glass fiber reinforced polymer tabs were bonded to both ends of the specimens using epoxy resin. The contact surfaces were sanded and cleaned before bonding to ensure adhesion quality. The tensile tests were performed without tabs.

Accelerated aging test

To simulate and accelerate the aging behavior of the CFRP materials in the low temperature Polar environment, the multi-factor equivalent environmental accelerated tests were designed and shown in Fig. 2, including the moisture adsorption test, freezing-thawing cyclic test, low temperature freezing test, and UV radiation test. The selection of test conditions is based on the natural environmental spectrum of Zhongshan Station in Antarctica, which is provided in the supporting information (Table S1). Two aging schemes were proposed in Fig. 2 of which the temperature of the moisture adsorption test was 80 and 45 ℃, respectively. Subsequently, the freezing-thawing cycles from -40 ℃ for 3 h to 20 ℃ for 3 h were performed. Then, a 24-hour low-temperature freezing test was carried out for 24 h. Finally, a 24-hour ultraviolet (UV) irradiation test was implemented. The aging tests were carried out for 1, 3, 6, 9, and 12 cycles with the above aging schemes.

To further elucidate the key environmental factors that driving performance degradation during multi-factor coupled aging, supplementary single-factor control experiments were conducted to characterize the moisture absorption behavior and interfacial shear strength retention of T800-CFRP composites under controlled temperature conditions (detailed in Supporting Information). The results reveal that moisture uptake and interfacial shear strength degradation are strongly temperature-dependent, with elevated temperature accelerating moisture diffusion and subsequent interfacial damage, while low-temperature suppresses these effects. Notably, the performance deterioration observed under these single-factor temperature-moisture conditions is significantly milder than that under the full multi-factor coupled aging protocol, providing direct evidence that the synergistic interaction of multiple environmental factors (moisture, temperature fluctuation, freeze-thaw, and UV radiation) is the primary driver of the pronounced material failure observed in this study.

To better align the experimental results with the targeted low-temperature/polar service environment, supplementary mechanical tests were conducted on T800-CFRP composites at 50 °C, -10 °C, and -70 °C, covering tensile, compression, interlaminar shear, impact, and flexural properties (detailed in Supporting Information). These supplementary data complement the room-temperature residual performance results, providing a more comprehensive understanding of the mechanical behavior of the composites under temperature ranges relevant to polar service conditions, and further strengthening the practical relevance of this study.

Mechanical test

After the multi-factor accelerated aging tests with different cycles, a series of mechanical property tests were performed on the aged specimens to evaluate the degradation behavior of the composite materials. These tests focus on the residual mechanical properties and long-term durability of composites after exposure to simulated polar environments. To ensure the accuracy of residual mechanical property characterization, all mechanical tests were conducted immediately after the completion of multi-factor coupled environmental aging treatments, without additional room-temperature storage.

Tensile tests were carried out using a universal testing machine (as shown in Fig. 3a) in accordance with the GB/T 1447-2005 [47], using dog-bone specimens to facilitate gripping and prevent premature failure at the clamping ends. During the test, the crosshead speed (tensile rate) was set to 2 mm/min, and the clamping hydraulic pressure was adjusted to 12 MPa to ensure that the specimens were firmly clamped without slippage or damage. Compression tests were performed following the GB/T 1148-2005 [48]. A special compression fixture (Fig. 3c) was used to prevent the specimens from buckling during the test. The loading speed of the testing machine was set to 1.3 mm/min.

Bending tests were performed using the same universal testing machine based on the GB/T 33621-2017 [49]. During the test, the span was set to 70 mm, and the loading speed was adjusted to 2 mm/min. Special bending fixtures (Fig. 3d and Fig. 3e) were used to apply the load uniformly on the specimens.

Izod impact tests were conducted using a pendulum impact testing machine (Fig. 3b) in accordance with the GB/T 1843-2008 [50]. Unnotched specimens were used to characterize the overall fracture toughness of the aged composites. An impact head with an energy of 5.5 J was selected for the test. Interlaminar shear tests were carried out using a universal testing machine in compliance with the Chinese National Standard GB/T 30969-2014 [51]. The span of the testing machine was set to 17 mm, and the loading speed was controlled at 1 mm/min to ensure that the shear failure occurred at the interlaminar interface of the composite materials.

All the mechanical tests for the aged samples were conducted at room temperature 25 ± 2 °C and relative humidity 50 ± 5%, to evaluate the residual mechanical properties following polar environmental aging. This approach is widely adopted and intended to characterize the long-term degradation and damage accumulation, as well as performance retention rate of composites under harsh service environments. Five replicate specimens were tested for each aging condition, and the average values are presented in the results.

Water adsorption test

The water absorption test was conducted as follows. Firstly, the specimens were dried in an

oven at 50 ± 2°C for 24 h. After removal and cooling to room temperature in a desiccator, their initial mass (m_0) was recorded. The initial mass m_0 was determined after the specimens were dried to a constant mass to ensure a stable dry state. The specimens were subsequently subjected to the moisture absorption conditioning outlined in Scheme A and B. Following each absorption cycle, the samples were removed and the surface moisture was carefully blotted with filter paper, and their mass was measured again before being returned to the conditioning environment. This procedure was repeated to monitor the evolution of the moisture absorption rate (equation 1) over multiple cycles.

$$M_i=\frac{m_i-m_0}{m_0}\times 100\% \quad (1)$$

where M_i is the moisture absorption rate of the specimen; m_i is the test mass of the specimen during testing.

Microscopic characterization

The macro-morphologies of the CFRPs after aging and mechanical test were observed by digital camera (Canon, EOS 850D). The surface micro-morphologies of the CFRP specimens, including the front and back sides, were characterized before and after aging using scanning electron microscopy (SEM, Quanta 250). Prior to observation, all specimens were dried and cleaned, and the same designated surface of each specimen was examined both before and after aging to ensure comparability. The SEM observations were performed under vacuum conditions using the SE2 mode with an accelerating voltage of 15 kV. Additionally, the tensile fracture surfaces of the samples were examined with SEM to evaluate the effect of aging on the failure mechanisms. Digital Image Correlation (DIC, Q400) was employed to characterize the strain evolution in the Y-direction during tensile testing. Prior to DIC measurement, random speckle patterns were carefully fabricated on the specimen surface using matte black and white spray paints to ensure measurement accuracy. The system was equipped with a 5 Megapixel camera operating at a frame rate of 25 Hz. The field of view (FOV) was approximately 12.8 mm × 9.6 mm, corresponding to a strain resolution better than 100 με under the present conditions.

The carbon chemical composition of CFRP specimens before and after multi-factor coupled environmental aging was characterized via a confocal Raman spectrometer (Renishaw in Via^{TM}) equipped with a 532 nm laser. Spectra were acquired over the range of 800-2000 cm^{-1} for the identification of carbon-related characteristic bands and confirmation of potential chemical changes.

Data availability statement

The raw/processed data required to reproduce these findings cannot be shared at this time as the data is related to an ongoing study.

Acknowledgment

The authors wish to acknowledgement the financial support of the Natural Science Foundation of China (52371080), Natural Science Foundation of Shandong province (ZR2024JQ028), the Youth Innovation Plan of Shandong Province (2022KJ002), and the Project of Taishan Scholars (tsqn202312107).

Author Contributions Statement

M.Z.: Conceptualization, Methodology Investigation, Writing-Original. W.L.: Validation, Formal Analysis. W.Y.: Methodology, Validation. W.W.: Software. J.L.: Methodology Investigation, Validation. H.L.: Methodology Investigation. C.M.: Review & Editing. Z.C.: Review & Editing, Funding Acquisition, Supervision. All authors reviewed the manuscript.

Competing Interest

The authors declare no competing financial or non-financial interests.

References

1. Han, Y., Xu, Q., Wang, Y.-Q. & Gao, H. Bionic CFRP for extreme applications: from natural structures to high-performance manufacturing. *Composites Part B* **311**, 113193 (2026).
2. Hao, Z. *et al.* Mechanical characteristics and application of CFRP cable anchor support structures in coastal area. *Ocean Eng.* **299**, 117366 (2024).
3. An, Q., Ming, W., Cai, X. & Chen, M. Effects of tool parameters on cutting force in orthogonal machining of T700/LT03A unidirectional carbon fiber reinforced polymer laminates. *J. Reinf. Plast. Compos.* **34**, 591-602 (2015).
4. Luo, K., Chen, L. & Liang, W. Structural health monitoring of carbon fiber reinforced polymer composite laminates for offshore wind turbine blades based on dual maximum correlation coefficient method. *Renew. Energy* **201**, 1163-1175 (2022).
5. Shao, Z., Liu, Z., Zhang, Y. & Zhu, X. Fatigue Life Prediction and Reliability Assessment of CFRP Adhesively Bonded Joints in Offshore Wind Turbine Blade Applications: A Physics‐Informed Data‐Driven Approach. *Qual. Reliab. Eng. Int.* **41**(2025).
6. Shen, M.-Y., Guo, Z.-H. & Feng, W.-T. A study on the characteristics and thermal properties of modified regenerated carbon fiber reinforced thermoplastic composite recycled from waste wind turbine blade spar. *Composites Part B* **264**, 110878 (2023).
7. Wang, Q. *et al.* Structure design and ultimate strength envelope of a modular carbon fiber-reinforced polymer (CFRP) laminate tube box on a 5000 ft deep-sea ultra large unmanned underwater vehicle. *Ocean Eng.* **313**, 119681 (2024).
8. Zhao, Q., Zhao, W. & Wu, Y. Constructing bi-functional Ce-MOF on carbon fiber endowing epoxy coating with excellent anti-corrosion and erosion wear resistance. *Carbon.* **214**, 14 (2023).
9. Zhang, X., Zhao, M., Xia, J. & Ge, T. Underwater implosion protection of a new concept composite structure for a deep-sea hollow ceramic sphere with CFRP shield. *Ocean Eng.* **306**, 19 (2024).
10. Qin, Z. *et al.* Effect of Thickness on the Uniaxial Compression Failure Behavior of CFRP Laminates. *Polymers.* **17**, 2518 (2025).
11. Li, Y. *et al.* Cryogenic mechanics and damage behaviors of carbon fiber reinforced polymer composites. *Composites Part A.* **169**, 16 (2023).
12. Liu, J. *et al.* Experimental study of notched tensile strength of large open-hole carbon fiber reinforced polymer laminates at low temperature. *Compos. Commun.* **39**, 101546 (2023).
13. Vigón, P., Argüelles, A., Lozano, M. & Viña, J. Fracture analysis under modes I and II of adhesive joints on CFRP in saline environment. *Npj Mater. Degrad.* **8**, 117 (2024).
14. Yu, H. & Xing, P. Moisture absorption characterization of carbon fiber-reinforced polymer using Fickian and non-Fickian models. *Polym. Compos.* **43**, 8935-8946 (2022).
15. Xiang, Z.D. & Jones, F.R. Thermal-spike-enhanced moisture absorption by polymer-matrix carbon-fibre composites. *Compos. Sci. Technol.* **57**, 451-461 (1997).
16. Korkees, F. Moisture absorption behavior and diffusion characteristics of continuous carbon fiber reinforced epoxy composites: a review. *Polym.-Plast. Technol. Mater.* **62**, 1789-1882 (2023).
17. Zhong, Y. & Joshi, S.C. Initiation of structural defects in carbon fiber reinforced polymer composites under hygrothermal environments. *J. Compos. Mater.* **50**, 1085-1097 (2016).

18. Pang, Y.Y., Wu, G., Wang, H.T., Su, Z.L. & He, X.Y. Experimental study on the bond behavior of the CFRP-steel interface under the freeze–thaw cycles. *Thin-Walled Struct.* **159**, 107233 (2020).
19. Cao, Q., Xu, J., Wu, Z. & Zhang, L. Performance of damaged concrete stub columns strengthened with post-tensioned CFRP under freezing-thawing environment. *Structures.* **47**, 544-556 (2023).
20. Li, W., Liu, W., Xu, W. & Ji, Y. Durability Investigation on CFRP Strengthened Cementitious Materials in Cold Region. *Polymers.* **14**, 2190 (2022).
21. Li, K., Zhou, A., Liu, T., Zou, D. & Yu, Z. Long-term performance and deterioration mechanism of novel hydrophobic coated fiber reinforced composite in marine environment. *Composites Part A.* **190**, 108716 (2025).
22. Sápi, Z. & Butler, R. Properties of cryogenic and low temperature composite materials – A review. *Cryogenics.* **111**, 103190 (2020).
23. Suo, H., Yiheng, W., Zhaohui, W., Cheng, H. & Luo, B. Modeling to investigate the mechanical degradation of carbon fiber-reinforced polymer composites subjected to salt-fog and ultraviolet radiation synergistic environment. *J. Mater. Sci.* **60**, 5847-5868 (2025).
24. Jang, J.H. *et al.* Long-term properties of carbon fiber-reinforced shape memory epoxy/polymer composites exposed to vacuum and ultraviolet radiation. *Smart Mater. Struct.* **28**, 115013 (2019).
25. Ding, J.C., Li. Experimental study on ultrasonic three-point bending fatigue of CFRP under ultraviolet radiation. *Eng. Fract. Mech.* **242**, 107435 (2021).
26. Dong, S. *et al.* Durability of carbon- and glass-fiber reinforced thermoplastic polymer composites: A literature review. *J. Build. Eng.* **98**, 111055 (2024).
27. Qin, G. *et al.* Influence of single or multi-factor coupling of temperature, humidity and load on the aging failure of adhesively bonded CFRP/aluminum alloy composite joints for automobile applications. *Int. J. Adhes. Adhes.* **123**, 103345 (2023).
28. Peng, H., Zhou, T., Shangguan, L. & Cheng, R. Effect of Temperature and Humidity Coupling on the Ageing Failure of Carbon Fiber Composite/Titanium Bonded Joints. *Polymers.* **16**, 952 (2024).
29. Ma, He, Hui & Xu. Effects of hygrothermal and thermal aging on the low-velocity impact properties of carbon fiber composites. *Adv. Compos. Mater.* **29**, 55-72 (2020).
30. Zhou, S., Yao XiongXu, LiangWang, LeiHui, Li. Study on the damage behavior of carbon fiber composite after low-velocity impact under hygrothermal aging. *J. Appl. Polym. Sci.* **138**, 50289 (2021).
31. Lei, Y., Kang, Z., Zhang, J., Sun, Y. & Zhang, B. Effect of freeze-thaw cycling on the mechanical properties of continuous carbon fiber-reinforced polyamide 6 composites. *Polym. Test.* **114**, 107704 (2022).
32. Chiang, Z.F.P. Experimental investigation of the synergistic effects of moisture and freeze-thaw cycles on carbon fiber vinyl-ester composites. *J. Compos. Mater.* **52**, 919-930 (2018).
33. Tan, C., Jiang, X., Qiang, X. & Fan, M. Flexural Performance of Carbon Fiber-Reinforced Polymer Prestressed Spun High-Strength Concrete Pile. *Appl. Sci.* **14**, 7170 (2024).
34. Scott, P., Toumpanaki, E. & Lees, J.M. Solution Uptake in Cylindrical Carbon-Fibre-Reinforced Polymer (CFRP) Tendons. *Adv. Polym. Technol.* **16**, 1981256 (2022).
35. Meng, M., Rizvi, M.J., Le, H.R. & Grove, S.M. Multi-scale modelling of moisture diffusion coupled with stress distribution in CFRP laminated composites. *Compos. Struct.* **138**, 295-304 (2016).
36. Kang, C. *et al.* Experimental investigation of friction between prepreg tape and compaction roller for prepreg tape hoop winding. *J. Reinf. Plast. Compos.* **37**, 853-862 (2018).

37. Murdy, P. *et al.* Hygrothermal Aging and Thermomechanical Characterization of As-Manufactured Tidal Turbine Blade Composites. *J. Mar. Sci. Eng.* **13**, 1790 (2025).
38. Ofoegbu, S.U., Quevedo, M.C., Bastos, A.C., Ferreira, M.G.S. & Zheludkevich, M.L. Electrochemical characterization and degradation of carbon fibre reinforced polymer in quiescent near neutral chloride media. *npj Mater. Degrad.* **6**, 49 (2022).
39. Wang, Y., Meng, Z., Zhu, W., Wan, B. & Bai, Y. Hygrothermal aging behavior and aging mechanism of carbon nanofibers/epoxy composites. *Constr. Build. Mater.* **294**, 123538 (2021).
40. Moghimi-Ardekani, A., Ivens, J. & Vuure, A.W.V. Fatigue behaviour of flax fibre reinforced thermoset composites under hygrothermal conditions. *Int. J. Fatigue* **200**, 109114 (2025).
41. Jinhao, W. *et al.* Study on tensile properties of carbon fiber reinforced AA7075 composite at high temperatures. *Mater. Sci. Eng. A.* **825**, 141931 (2021).
42. Yang, Y., Jiang, Y., Liang, H., Yin, X. & Huang, Y. Study on Tensile Properties of CFRP Plates under Elevated Temperature Exposure. *Materials.* **12**, 1995 (2019).
43. Jiang, F. *et al.* Effect of freeze-thaw cycles on tensile properties of CFRP, bond behavior of CFRP-concrete, and flexural performance of CFRP-strengthened concrete beams. *Cold. Reg. Sci. Technol.* **194**, 103461 (2022).
44. Yu, H., Zhao, H. & Shi, F. Bending Performance and Reinforcement of Rocker Panel Components with Unidirectional Carbon Fiber Composite. *Materials.* **12**, 3164- (2019).
45. Jin, L. *et al.* Size effect in shear failure of RC beams reinforced with CFRP sheets: Influences of CFRP adhesion angle and shear-span ratio. *Eng. Struct.* **326**, 119543 (2025).
46. Vitale, P., Francucci, G.M., Rapp, H. & Stocchi, A.L. Shear response of ultra-lightweight CFRP cores. *Elsevier.* **238**, 111879 (2020).
47. Federation, C.B.M. Fiber-reinforced plastics composites-Determination of tensile properties. Vol. GB/T 1447-2005 (China, 2005).
48. Federation, C.B.M. Fiber-reinforced plastics composites-Determination of compressive properties. Vol. GB/T 1448-2005 (China, 2005).
49. Council, C.N.T.a.A. Test method for bending properties of 3D braided fabric and its polymer matrix composites. Vol. GB/T 33621-2017 (China, 2017).
50. Federation, C.P.a.C.I. Plastics - Determination of izod impact strength. Vol. GB/T 1843-2008 (China, 2008).
51. Federation, C.B.M. Test method for short-beam shear strength of polymer matrix composite materials. Vol. GB/T 30969-2014 (China, 2014).

Figure Captions

Fig. 1. Schematic diagram of the CFRP sample dimensions used for tensile test (a), compression test (b), bending test (c), izod impact test (d), and shear test (e).

Fig. 2. Two testing schemes for the multifactor equivalent environmental acceleration tests that simulated Polar marine environments.

Fig. 3. Macro images of the testing apparatus: (a) Universal testing machine, (b) Izod impact testing machine, (c) Compression test fixture, (d) Bending test fixture, (e) Schematic diagram of bending test fixture: 1 - specimen support; 2 - upper loading indenter; 3 - specimen; L-specimen length; l - span; h - specimen thickness; R - radius of the upper loading indenter(6 mm); r - radius of the support(10 mm); P - applied load.

Fig. 4. Representative morphologies of the composite materials after tensile testing: (a) T700-CFRP before aging; (b) T700-CFRP after 12 aging cycles; (c) T800-CFRP before aging; (d) T800-CFRP after 12 aging cycles.

Fig. 5. Tensile stress-strain curves of composite materials after different aging cycles: (a) T700-CFRP after aging under scheme A; (b) T700-CFRP after aging under scheme B; (c) T800-CFRP after aging under scheme A; (d) T800-CFRP after aging under scheme B; **The tensile strength retention rate of composite materials varies with aging cycles:** (e) T700-CFRP; (f) T800-CFRP.

Fig. 6. DIC analysis of 12-cycle aged T800-CFRP specimens showing Y-direction (vertical) strain evolution during tensile test at different loading stages: 0-32 s (initial elastic stage), 32-64 s (crack initiation stage), and 64-80 s (final fracture stage).

Fig. 7. Representative morphologies of the composite materials after compression testing: (a) T700-CFRP before aging; (b) T700-CFRP after 12 aging cycles; (c) T800-CFRP before aging; (d) T800-CFRP after 12 aging cycles.

Fig. 8. Compressive stress-strain curve of composite materials after different aging cycles: (a) T700-CFRP after aging under scheme A; (b) T700-CFRP after aging under scheme B; (c) T800-CFRP after aging under scheme A; (d) T800-CFRP after aging under scheme B; **The compressive strength retention rate of composite materials varies with aging cycles:** (e) T700-CFRP; (f) T800-CFRP.

Fig. 9. Representative morphologies of the composite materials after bending testing: (a) T700-CFRP before aging; (b) T700-CFRP after 12 aging cycles; (c) T800-CFRP before aging; (d) T800-CFRP after 12 aging cycles.

Fig. 10. Bending load-deflection curve of composite materials after different aging cycles: (a) T700-CFRP after aging under scheme A; (b) T700-CFRP after aging under scheme B; (c) T800-CFRP after aging under scheme A; (d) T800-CFRP after aging under scheme B; **The bending strength retention rate of composite materials varies with aging cycles:** (e) T700-CFRP; (f) T800-CFRP.

Fig. 11. Representative morphologies of the composite materials after Izod impact test: (a) T700-CFRP before aging; (b) T700-CFRP after 12 aging cycles; (c) T800-CFRP before aging; (d) T800-CFRP after 12 aging cycles.

Fig. 12. Shear failure morphology of CFRP composite specimens at 0~12 cycles of different multifactor aging.

Fig. 13. The interlayer shear strength retention rate of composite materials varies with aging cycles: (a) T700-CFRP; (b) T800-CFRP.

Fig. 14. Changes in moisture adsorption rate of two CFRPs during 12 cycles of different multifactor aging: (a) T700-CFRP subjected to Scheme A; (b) T700-CFRP subjected to Scheme B; (c) T800-CFRP subjected to Scheme A; (d) T800-CFRP subjected to Scheme B.

Fig. 15. Raman spectra of T800-CFRP specimens after multifactorial coupled environmental aging treatment under schemes A and B.

Fig. 16. Representative surface morphologies of T800-CFRP specimens before and after multifactorial coupled environmental aging treatment: (a) not aged front surface, (b) front surface after Scheme A, (c) front surface after Scheme B, (d) not aged back surface, (e) back surface after Scheme A, (f) back surface after Scheme B.

Fig. 17. Tensile fracture morphology of T800-CFRP composite specimens before and after multifactorial coupled environmental aging treatment: (a) not aged, (b) after Scheme A, (c)after Scheme B.

Fig. 18. Strength retention rate of two composite materials after aging following tensile, compressive, bending, and shear tests.

Fig. 19. Multifactorial environmental failure mechanism diagram for CFRP composite

materials: (a) Hygrothermal environment, (b) Freezing-thawing environment, (c) Low temperature environment, (d) Low temperature environment.

Table Captions

Table 1 The average tensile strength and its retention rate of T700 and T800 composite materials after ageing with different testing schemes for different cycles

Table 2 The average compressive strength and its retention rate of T700 and T800 composite materials after ageing with different testing schemes for different cycles

Table 3 The average bending strength and its retention rate of T700 and T800 composite materials after ageing with different testing schemes for different cycles

Table 4 The average izod impact test data of T700 and T800 composite materials after ageing with different testing schemes for different cycles

Table 5 The average interlayer shear strength and its retention rate of T700 and T800 composite materials after ageing with different testing schemes for different cycles

Table 1 The average tensile strength and its retention rate of T700 and T800 composite materials after ageing with different testing schemes for different cycles

Cycle Period		Not aged	1	3	6	9	12
T700-CFRP	Tensile strength /MPa	968.7	953.3	913.7	854.3	873.0	835.7
after aging	Standard deviation	15.9	44.2	58.5	17.0	16.5	12.0
under scheme A	Strength retention rate /%	/	98.4	94.3	88.2	90.1	86.2
T700-CFRP	Tensile strength /MPa	968.7	955.7	982.4	898.3	853.7	826.3
after aging	Standard deviation	24.2	35.2	27.3	36.1	17.0	49.6
under scheme B	Strength retention rate /%	/	98.7	/	92.7	88.1	85.3
T800-CFRP	Tensile strength /MPa	985.7	934.3	956.7	922.3	914.3	871.7
after aging	Standard deviation	15.9	41.3	35.8	40.3	36.6	39.1
under scheme A	Strength retention rate /%	/	94.8	97.1	93.6	92.8	88.4
T800-CFRP	Tensile strength /MPa	985.7	951.0	938.0	921.0	924.3	919.3
after aging	Standard deviation	24.2	16.5	37.5	87.0	43.2	10.1
under scheme B	Strength retention rate /%	/	96.5	95.2	93.4	93.8	93.2

Table 2 The average compressive strength and its retention rate of T700 and T800 composite materials after ageing with different testing schemes for different cycles

Cycle Period		Not aged	1	3	6	9	12
T700-CFRP	Compressive strength /MPa	531.3	509.7	476.3	464.7	413.3	378.0
after aging	Standard deviation	63.4	8.96	4.51	29.9	38.1	75.9
under scheme A	Strength retention rate /%	/	95.9	89.6	87.4	77.8	71.1
T700-CFRP	Compressive strength /MPa	531.3	518.3	503.7	490.0	463.3	388.0
after aging	Standard deviation	63.4	41.5	22.4	27.7	79.4	44.0
under scheme B	Strength retention rate /%	/	97.5	94.8	92.2	87.2	73.0
T800-CFRP	Compressive strength /MPa	713.3	669.0	661.3	641.0	654.3	646.7
after aging	Standard deviation	7.51	29.1	47.9	23.6	45.2	26.7
under scheme A	Strength retention rate /%	/	93.8	92.7	89.9	91.7	90.6
T800-CFRP	Compressive strength /MPa	713.3	681.7	683.0	683.3	661.7	650.3
after aging	Standard deviation	7.51	24.8	51.6	22.4	47.4	53.2
under scheme B	Strength retention rate /%	/	95.6	95.7	95.8	92.8	91.2

Table 3 The average bending strength and its retention rate of T700 and T800 composite materials after ageing with different testing schemes for different cycles

Cycle Period		Not aged	1	3	6	9	12
T700-CFRP after aging under scheme A	Bending strength /MPa	854.3	778.3	716.3	561.0	540.0	498.3
	Standard deviation	41.7	36.9	80.2	87.8	89.6	43.1
	Strength retention rate /%	/	91.1	83.8	65.7	63.2	58.3
T700-CFRP after aging under scheme B	Bending strength /MPa	854.3	787.0	721.7	612.0	537.0	527.0
	Standard deviation	41.7	34.9	92.8	64.5	53.7	61.9
	Strength retention rate /%	/	92.1	84.5	71.6	62.9	61.7
T800-CFRP after aging under scheme A	Bending strength /MPa	805	797.0	783.0	763.0	718.3	702.7
	Standard deviation	32.2	9.64	8.19	46.0	28.4	42.0
	Strength retention rate /%	/	99.0	97.3	94.8	89.2	87.3
T800-CFRP after aging under scheme B	Bending strength /MPa	805	801.3	788.0	772.3	722.3	712.3
	Standard deviation	32.2	7.51	55.3	50.5	41.6	67.7
	Strength retention rate /%	/	99.5	97.9	95.9	89.7	88.5

Table 4 The average izod impact test data of T700 and T800 composite materials after ageing with different testing schemes for different cycles

Cycle Period		Not aged	1	3	6	9	12
T700-CFRP after aging under scheme A	Energy absorbed (J)	2.8862	2.8876	2.8869	2.8863	2.8798	2.8796
	Impact strength (kJ/m^2)	72.154	72.159	72.172	72.157	71.996	71.991
T700-CFRP after aging under scheme B	Energy absorbed (J)	2.8862	2.8882	2.8860	2.8834	2.8862	2.8820
	Impact strength (kJ/m^2)	72.154	72.205	72.151	72.086	72.155	72.049
T800-CFRP after aging under scheme A	Energy absorbed (J)	2.8582	2.8405	2.8612	2.8841	2.8190	2.8233
	Impact strength (kJ/m^2)	71.455	71.031	71.529	72.103	70.476	70.559
T800-CFRP after aging under scheme B	Energy absorbed (J)	2.8582	2.8585	2.8573	2.8709	2.8406	2.8287
	Impact strength (kJ/m^2)	71.455	71.464	71.433	71.772	71.014	70.717

Table 5 The average interlayer shear strength and its retention rate of T700 and T800 composite materials after ageing with different testing schemes for different cycles

Cycle Period		Not aged	1	3	6	9	12
T700-CFRP	Interlayer Shear Strength /MPa	43.0	28.3	26.5	23.9	23.7	23.7
after aging	Standard deviation	2.56	2.74	4.34	0.25	1.37	2.06
under scheme A	Strength retention rate /%	/	65.8	61.6	55.6	55.1	55.1
T700-CFRP	Interlayer Shear Strength /MPa	43.0	28.1	26.4	26.5	26.1	26.1
after aging	Standard deviation	2.56	0.83	3.87	2.95	3.69	2.62
under scheme B	Strength retention rate /%	/	65.3	61.3	61.6	60.7	60.4
T800-CFRP	Interlayer Shear Strength /MPa	45.5	37.5	39.7	40.8	37.5	34.7
after aging	Standard deviation	1.25	1.76	1.25	3.48	0.61	0.30
under scheme A	Strength retention rate /%	/	82.4	87.3	89.6	82.4	76.3
T800-CFRP	Interlayer Shear Strength /MPa	45.5	37.2	36.6	37.1	37.4	36.2
after aging	Standard deviation	1.25	1.40	2.31	2.76	0.57	0.60
under scheme B	Strength retention rate /%	/	81.7	80.4	81.5	82.3	79.5

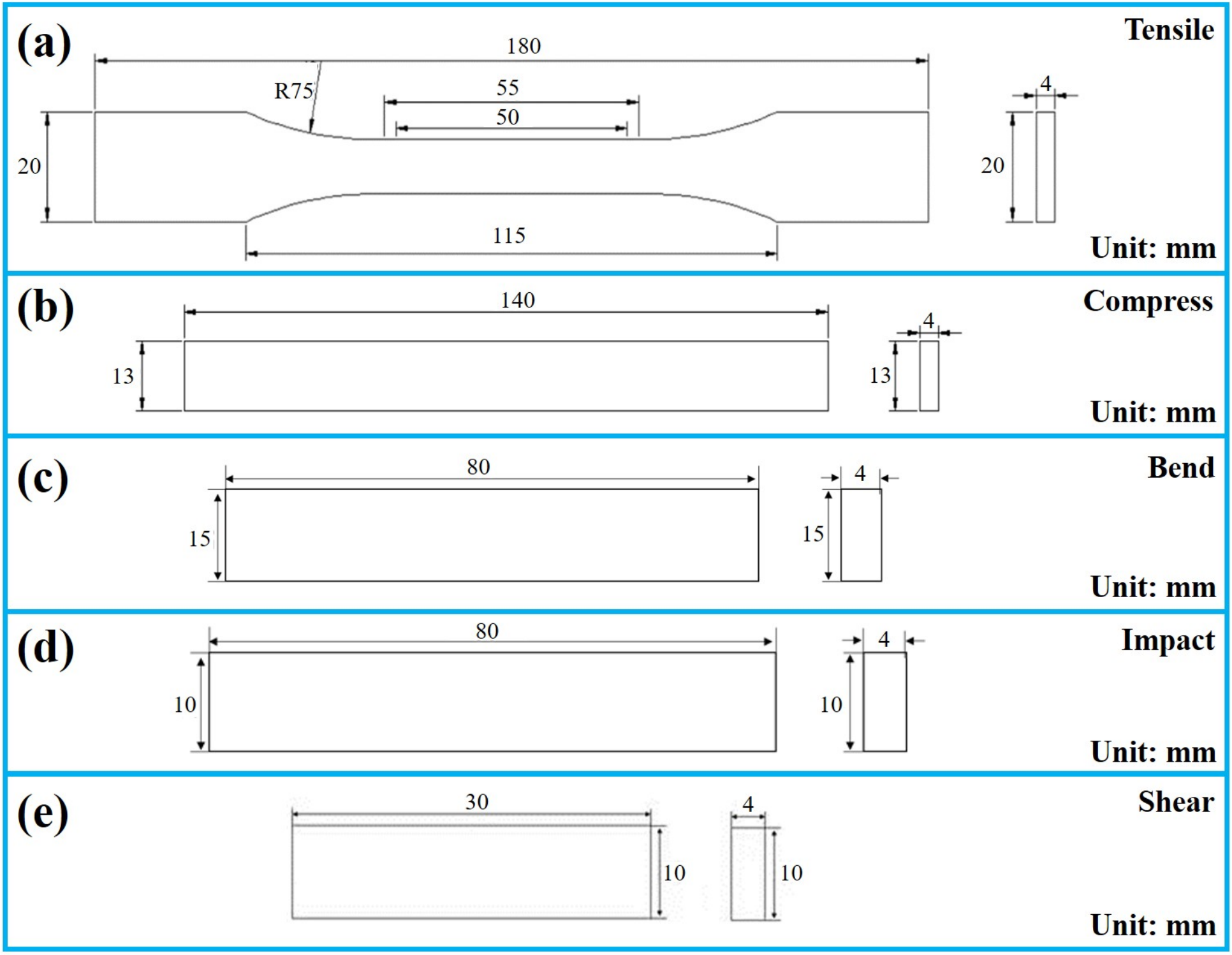
(a)
Tensile
180
R75
55
50
20
4
20
115
Unit: mm
(b)
Compress
140
4
13
13
Unit: mm
(c)
Bend
80
4
15
15
Unit: mm
(d)
Impact
80
4
10
10
Unit: mm
(e)
Shear
30
4
10
10
Unit: mm

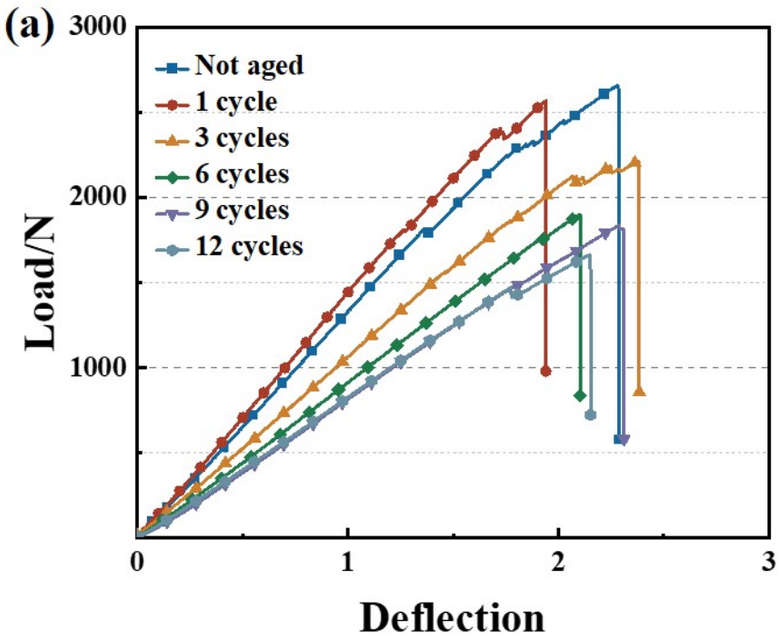
(a)
Not aged
1 cycle
3 cycles
6 cycles
9 cycles
12 cycles
Load/N
Deflection

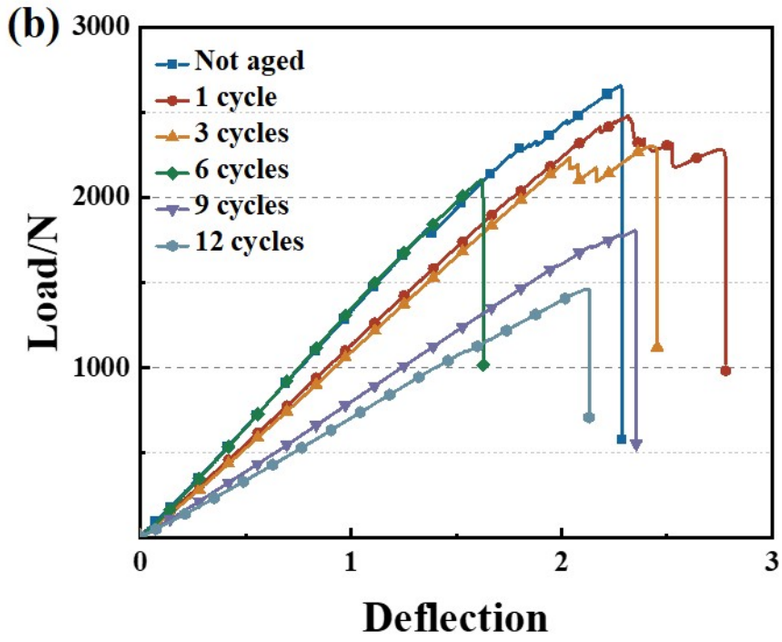
(b)
Not aged
1 cycle
3 cycles
6 cycles
9 cycles
12 cycles
Load/N
Deflection

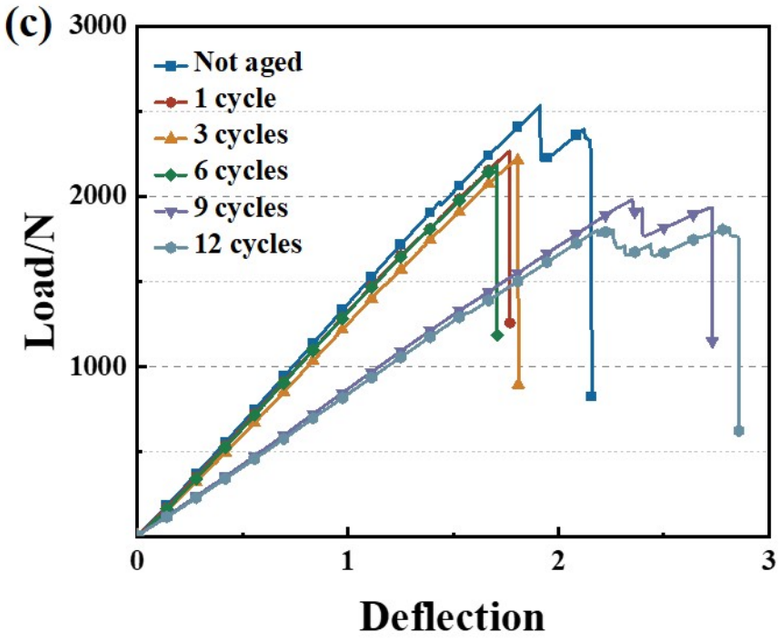
(c)
Not aged
1 cycle
3 cycles
6 cycles
9 cycles
12 cycles
Load/N
Deflection

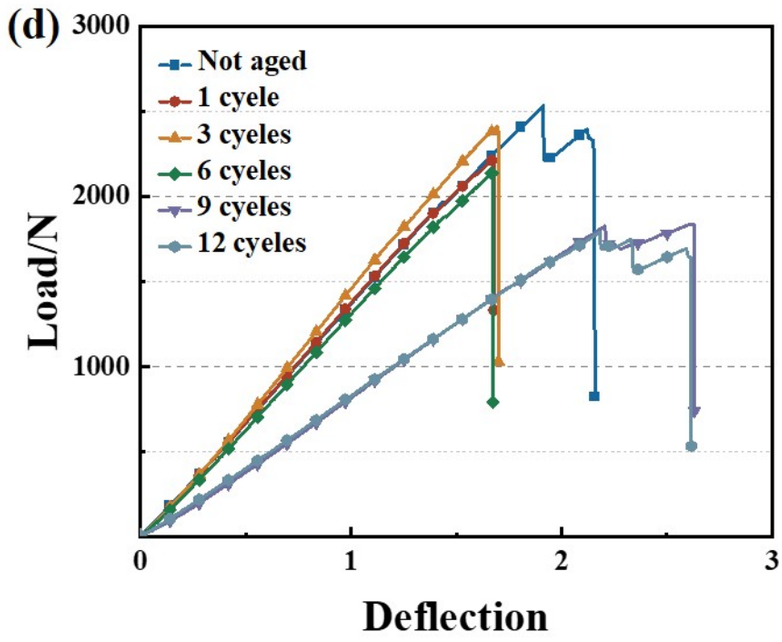
(d)
Not aged
1 cyele
3 cyeles
6 cyeles
9 cyeles
12 cyeles
Load/N
Deflection

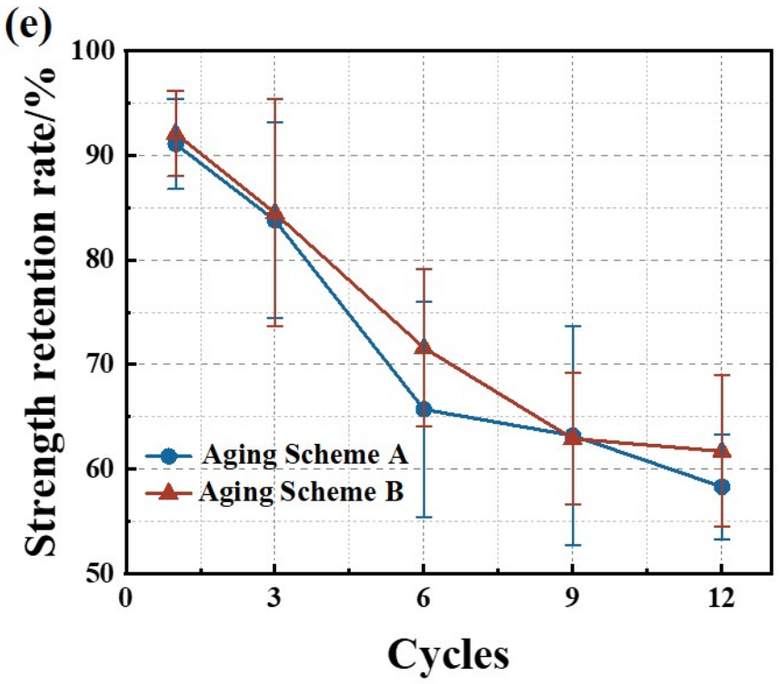
(e)
Aging Scheme A
Aging Scheme B
Strength retention rate/%
Cycles

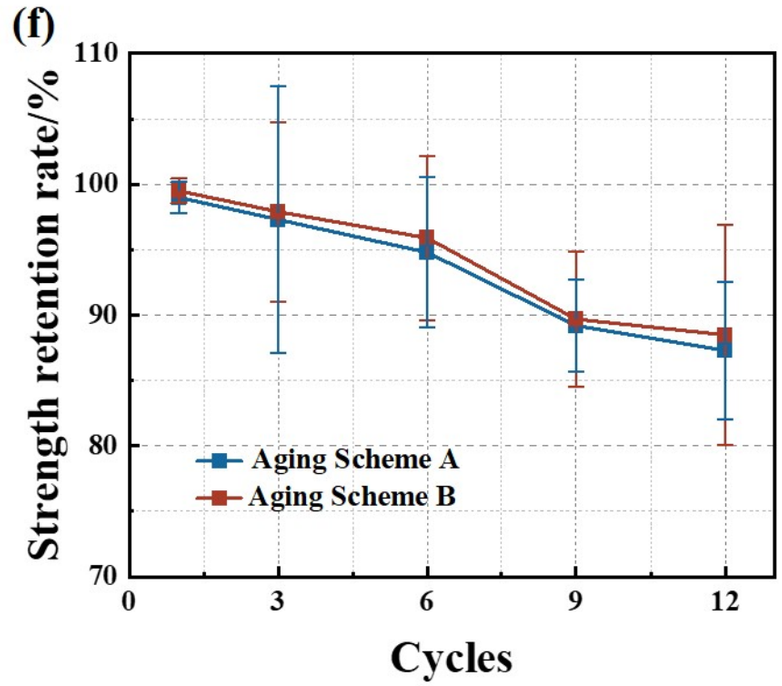
(f)
Aging Scheme A
Aging Scheme B
Strength retention rate/%
Cycles

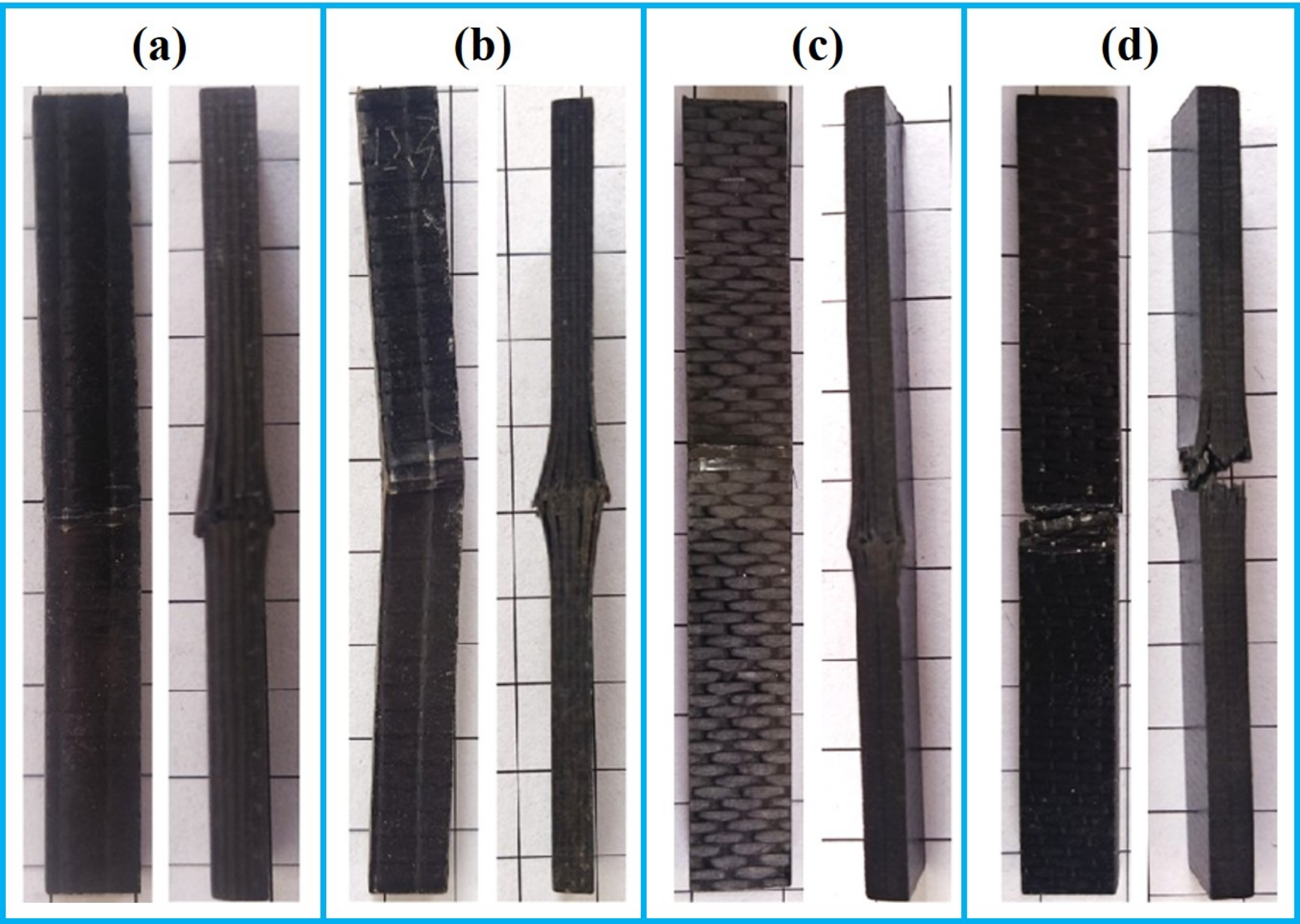
(a)
(b)
(c)
(d)

		T700-CFRP	T800-CFRP
Scheme A	Not aged		
	1 cycle		
	3 cycles	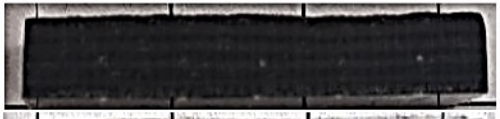	
	6 cycles		
	9 cycles		
	12 cycles		
Scheme B	Not aged		
	1 cycle		
	3 cycles		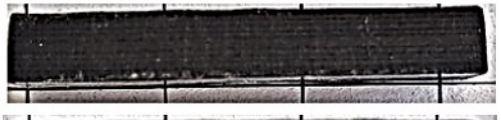
	6 cycles		
	9 cycles		
	12 cycles		

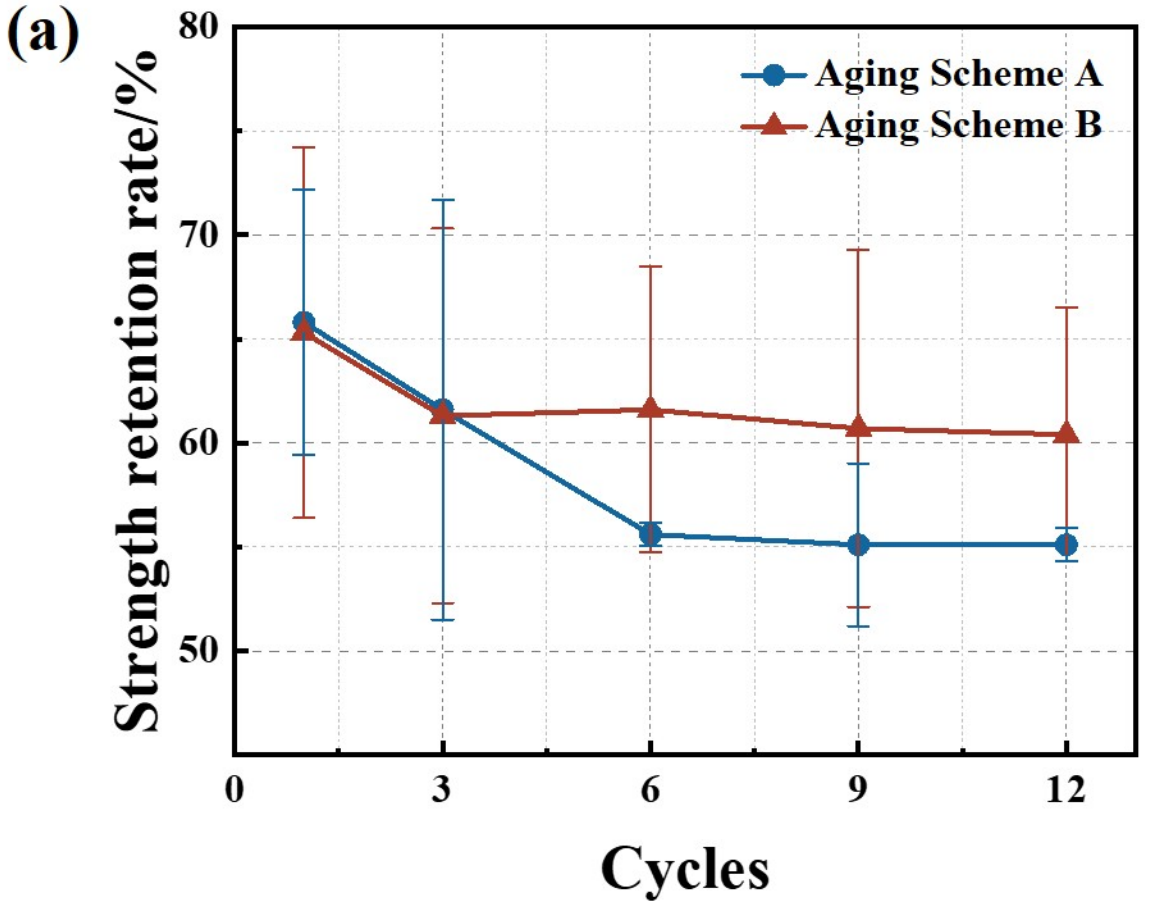
(a)
Strength retention rate/%
80
70
60
50
0
3
6
9
12
Cycles
Aging Scheme A
Aging Scheme B

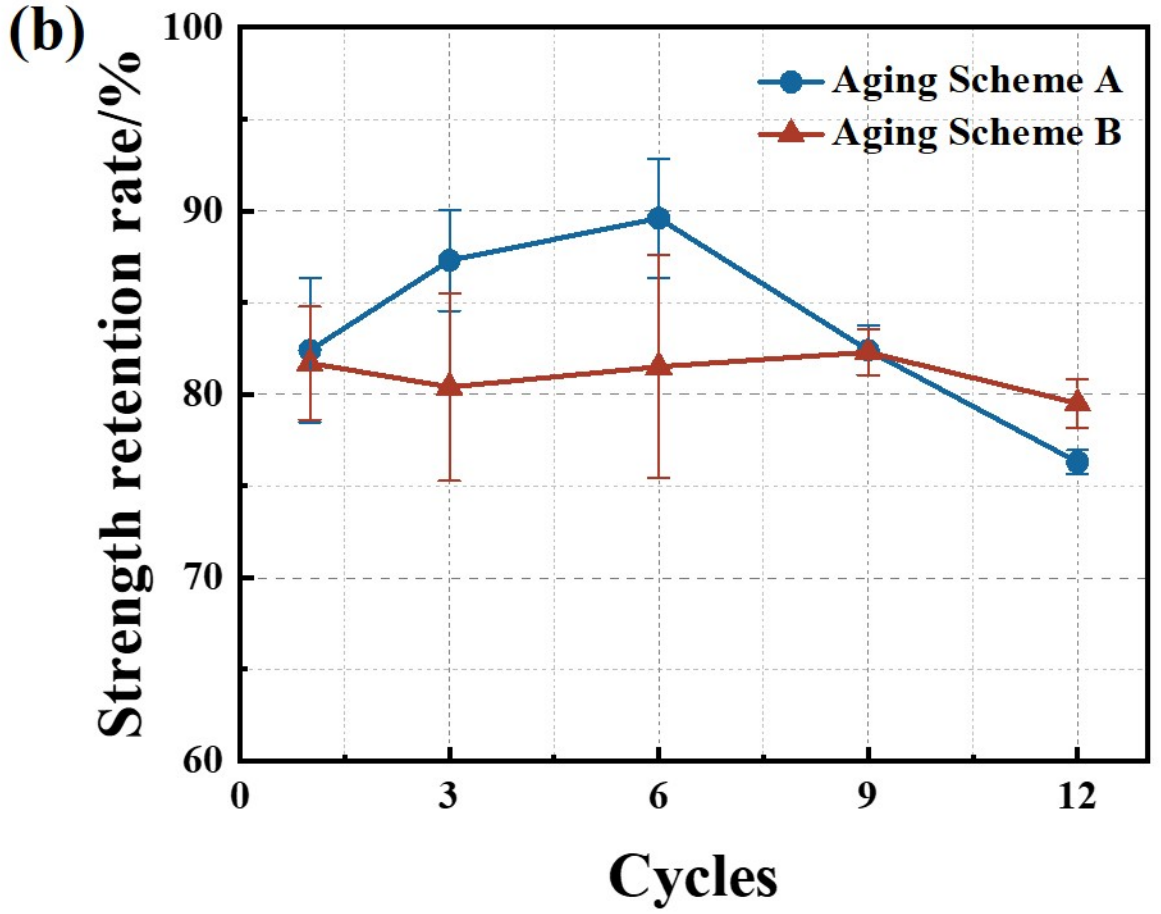
(b)
Strength retention rate/%
100
90
80
70
60
0
3
6
9
12
Cycles
Aging Scheme A
Aging Scheme B

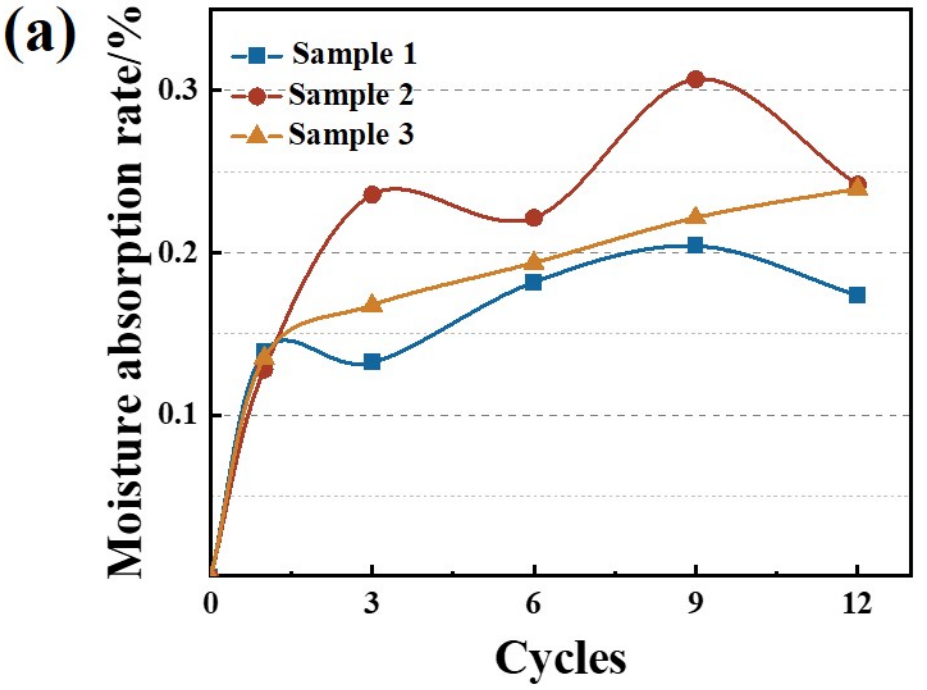
(a)
Sample 1
Sample 2
Sample 3
Moisture absorption rate/%
0.1
0.2
0.3
0
3
6
9
12
Cycles

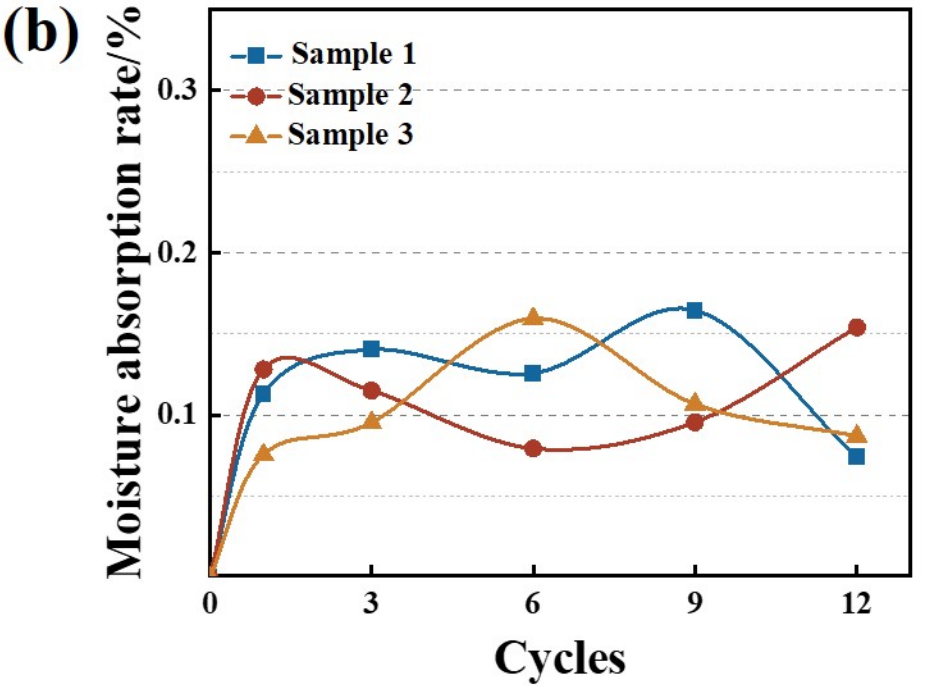
(b)
Sample 1
Sample 2
Sample 3
Moisture absorption rate/%
0.1
0.2
0.3
0
3
6
9
12
Cycles

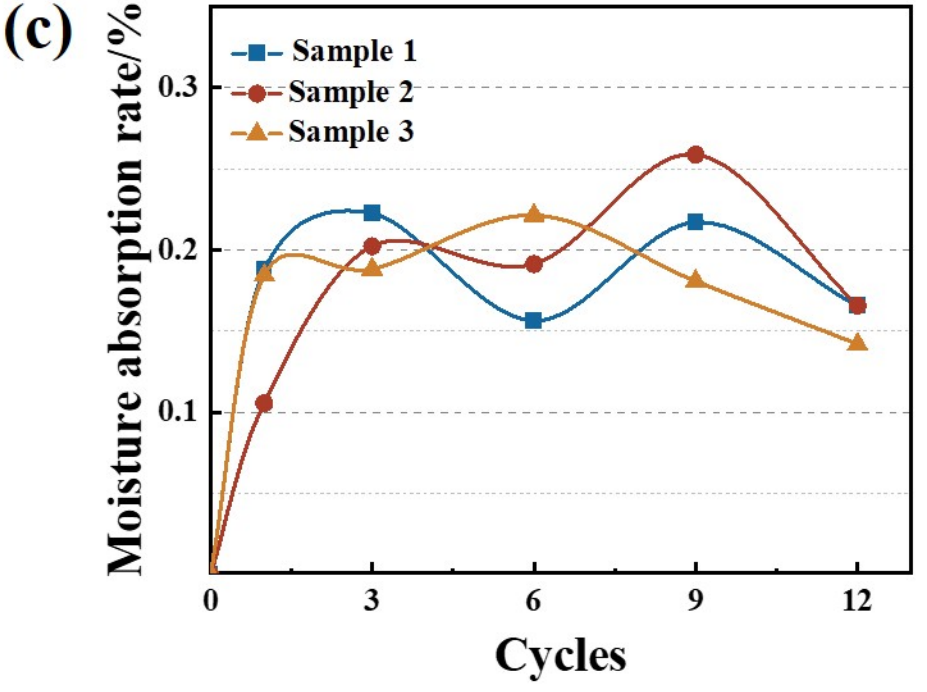
(c)
Sample 1
Sample 2
Sample 3
Moisture absorption rate/%
0.1
0.2
0.3
0
3
6
9
12
Cycles

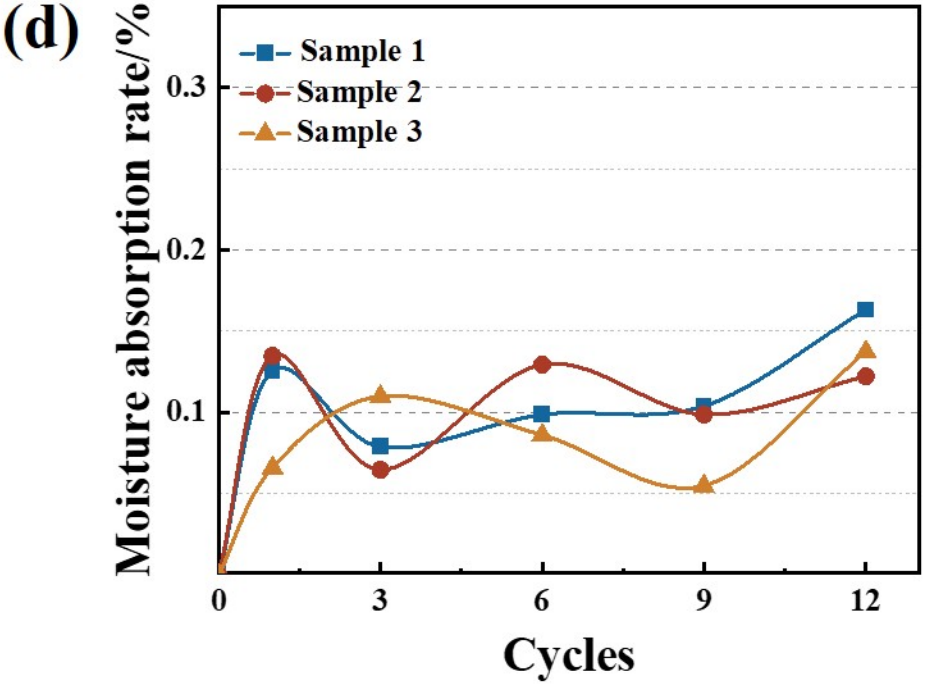
(d)
Sample 1
Sample 2
Sample 3
Moisture absorption rate/%
0.1
0.2
0.3
0
3
6
9
12
Cycles

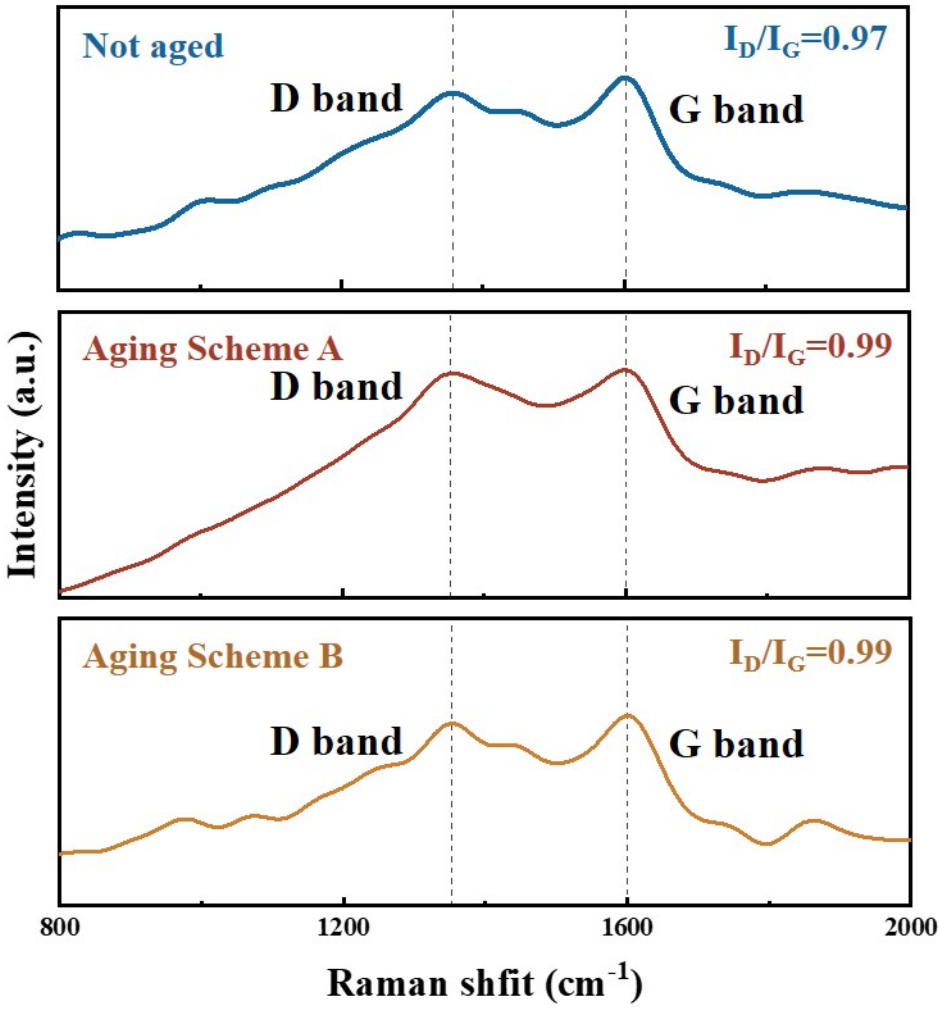
Not aged
I_D/I_G=0.97
D band
G band
Aging Scheme A
I_D/I_G=0.99
D band
G band
Aging Scheme B
I_D/I_G=0.99
D band
G band
Intensity (a.u.)
800
1200
1600
2000
Raman shfit (cm^{-1})

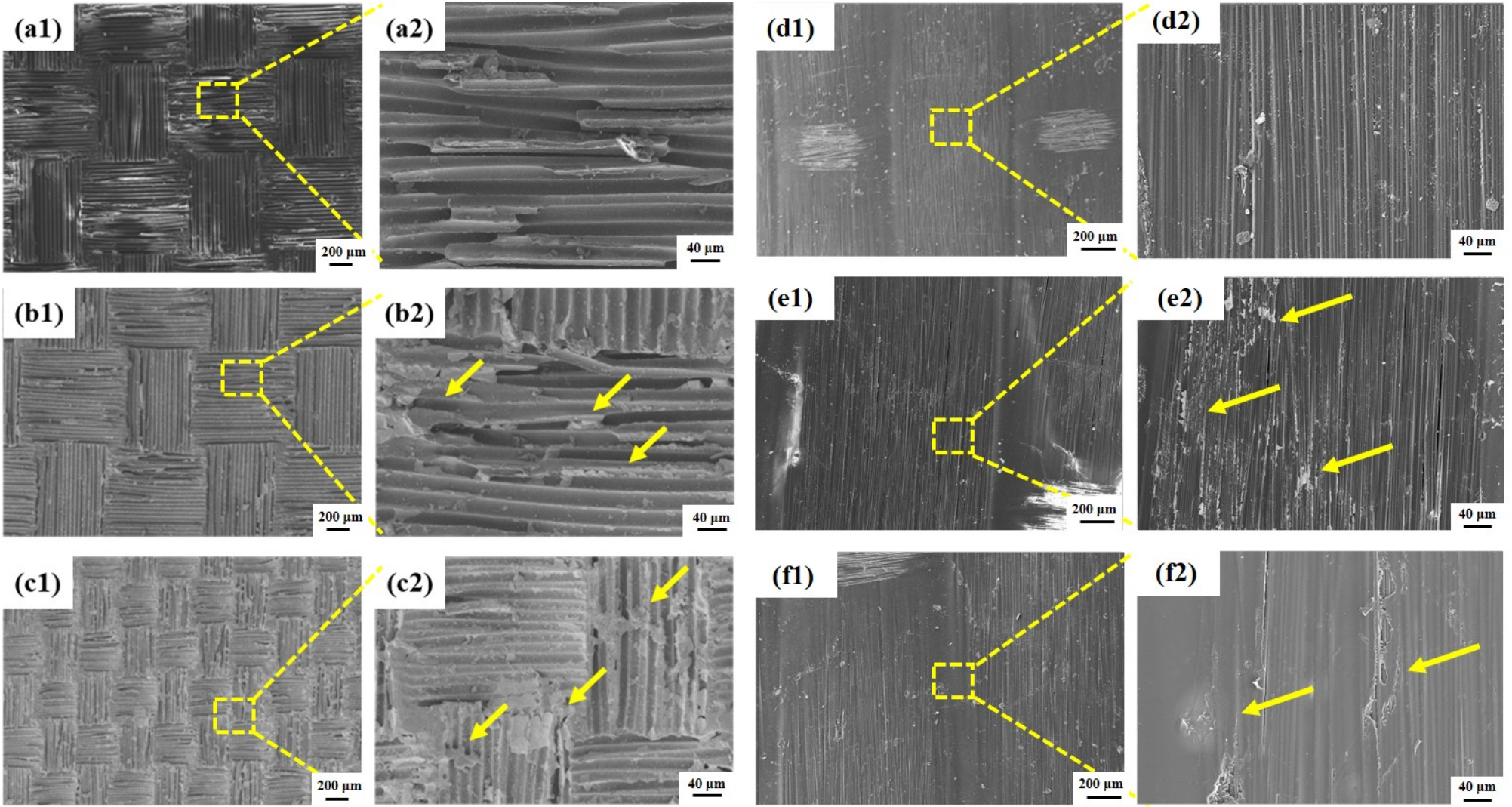
(a1)
200 μm
(a2)
40 μm
(b1)
200 μm
(b2)
40 μm
(c1)
200 μm
(c2)
40 μm
(d1)
200 μm
(d2)
40 μm
(e1)
200 μm
(e2)
40 μm
(f1)
200 μm
(f2)
40 μm

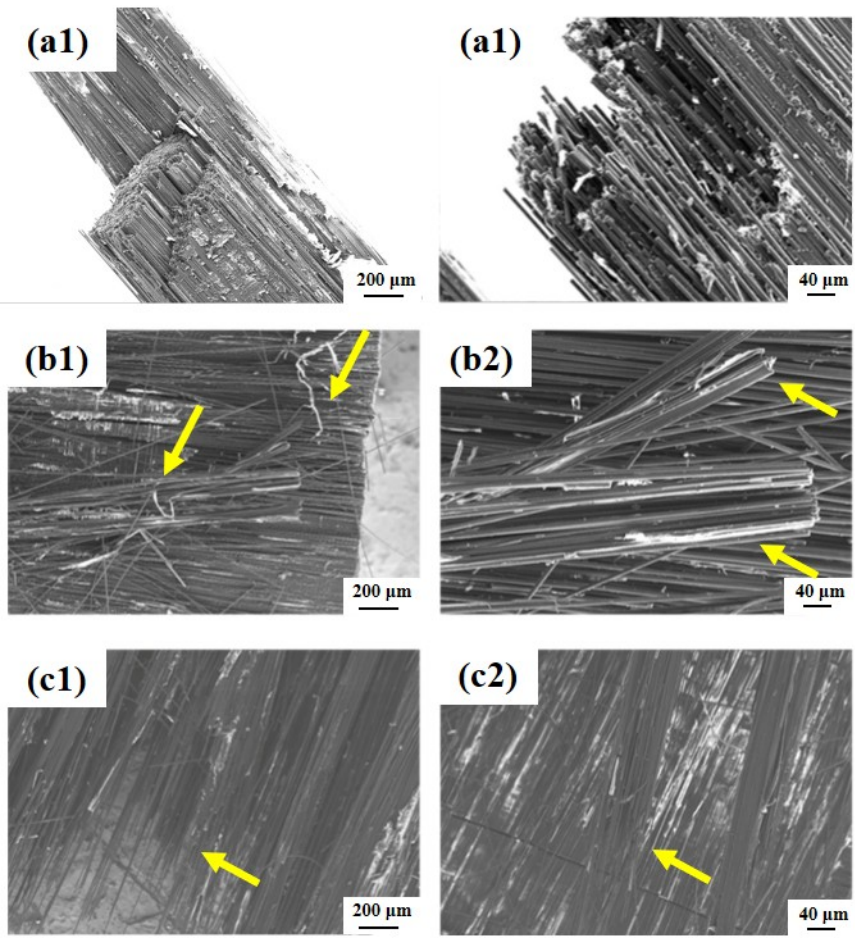
(a1)
200 μm
(a1)
40 μm
(b1)
200 μm
(b2)
40 μm
(c1)
200 μm
(c2)
40 μm

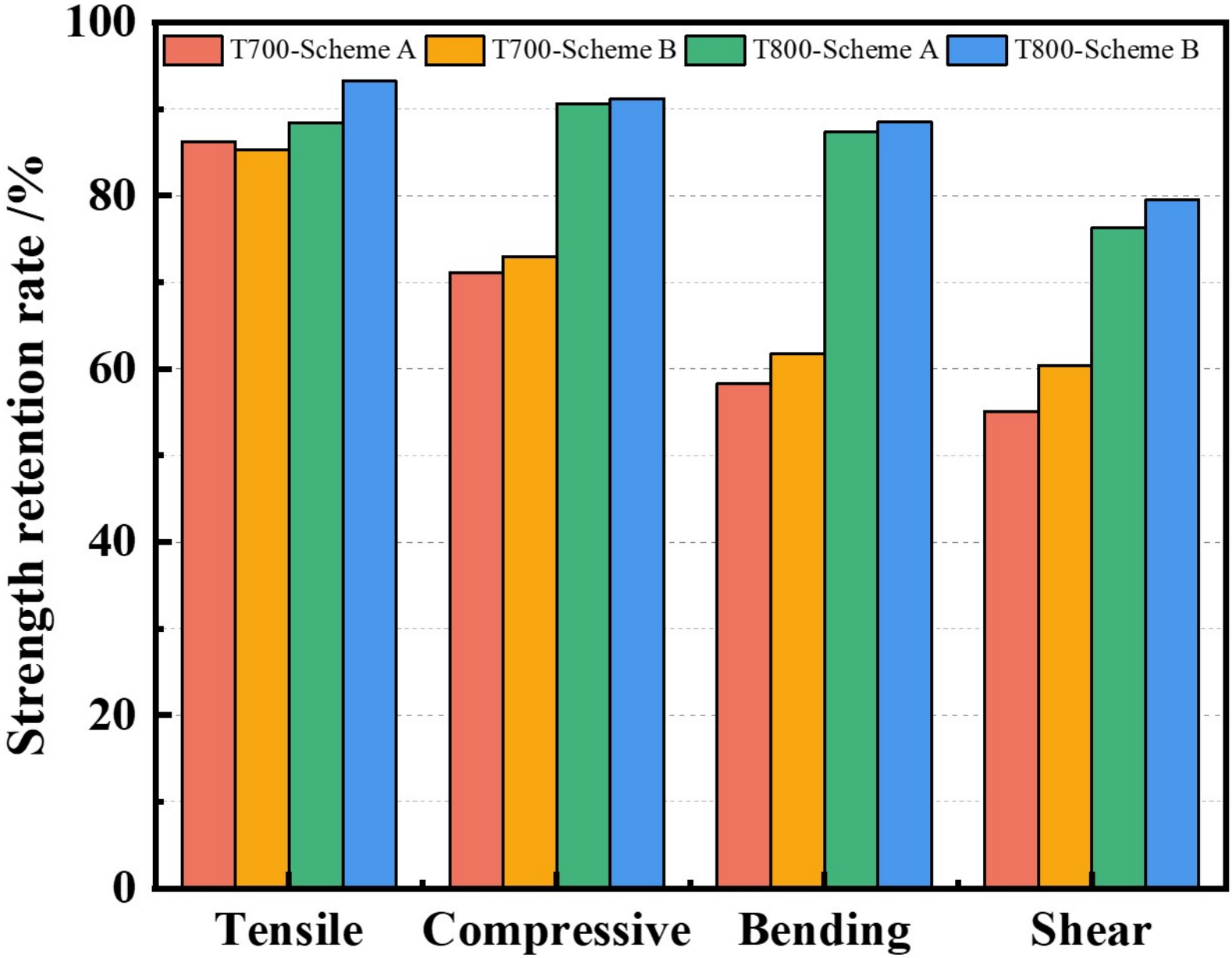
T700-Scheme A
T700-Scheme B
T800-Scheme A
T800-Scheme B
Strength retention rate /%
100
80
60
40
20
0
Tensile
Compressive
Bending
Shear

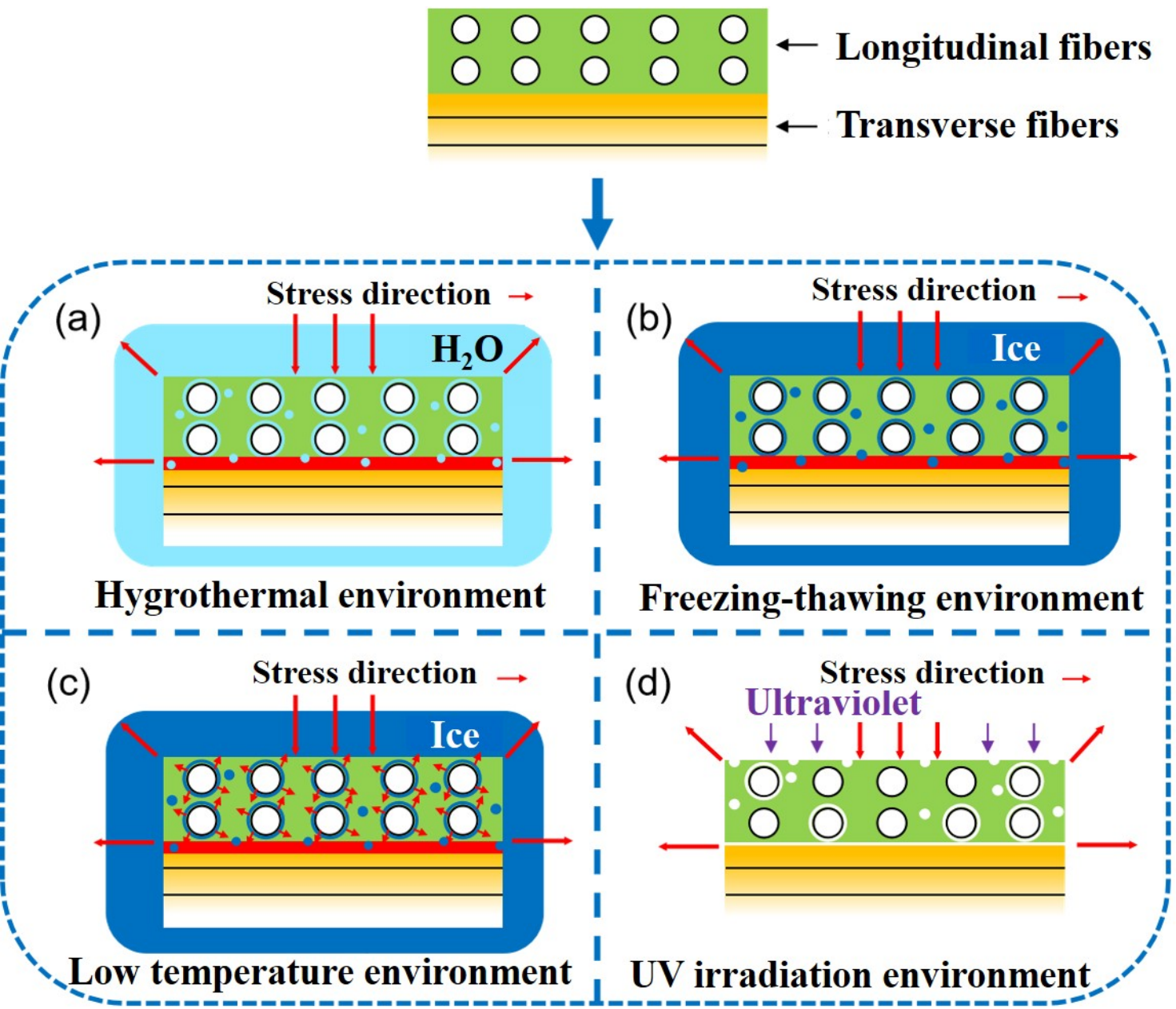
Longitudinal fibers
Transverse fibers
(a)
Stress direction
H_2O
Hygrothermal environment
(b)
Stress direction
Ice
Freezing-thawing environment
(c)
Stress direction
Ice
Low temperature environment
(d)
Stress direction
Ultraviolet
UV irradiation environment

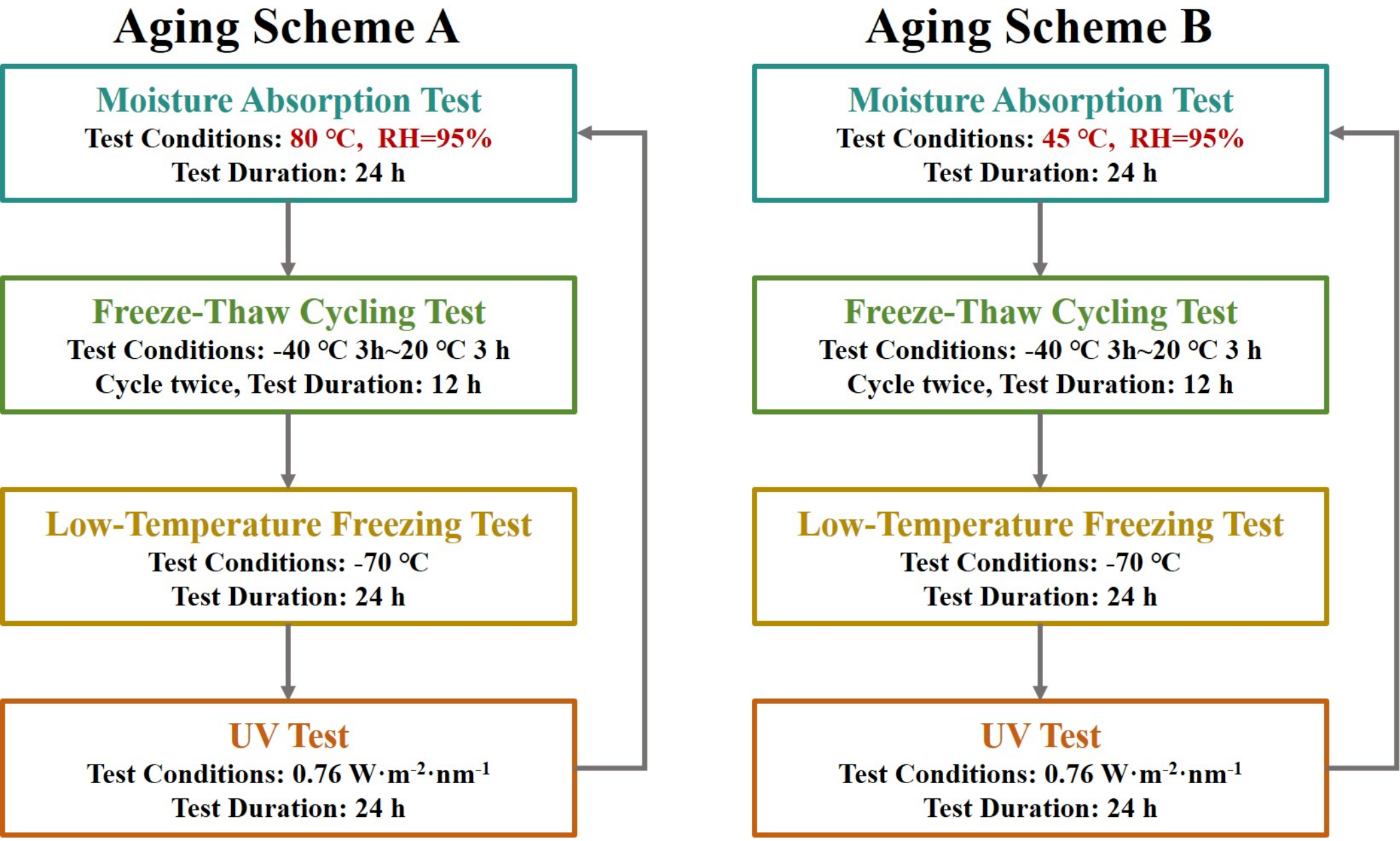
Aging Scheme A
Moisture Absorption Test
Test Conditions: 80 °C, RH=95%
Test Duration: 24 h
Freeze-Thaw Cycling Test
Test Conditions: -40 °C 3h~20 °C 3 h
Cycle twice, Test Duration: 12 h
Low-Temperature Freezing Test
Test Conditions: -70 °C
Test Duration: 24 h
UV Test
Test Conditions: 0.76 W·m-2·nm-1
Test Duration: 24 h
Aging Scheme B
Moisture Absorption Test
Test Conditions: 45 °C, RH=95%
Test Duration: 24 h
Freeze-Thaw Cycling Test
Test Conditions: -40 °C 3h~20 °C 3 h
Cycle twice, Test Duration: 12 h
Low-Temperature Freezing Test
Test Conditions: -70 °C
Test Duration: 24 h
UV Test
Test Conditions: 0.76 W·m-2·nm-1
Test Duration: 24 h


(a)
S/AS


(b)


(b-1)

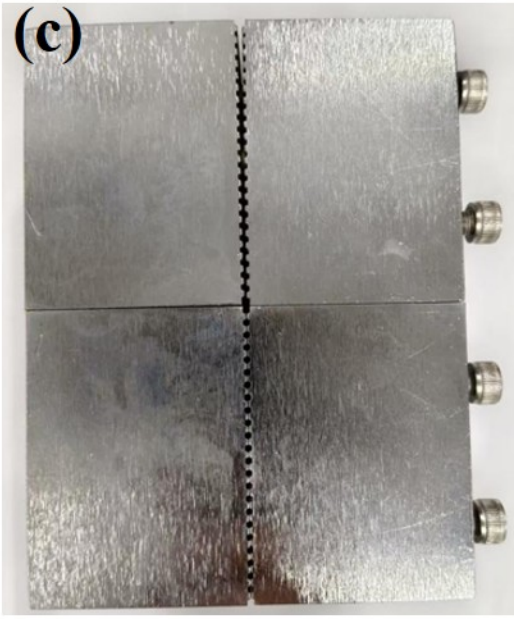
(c)

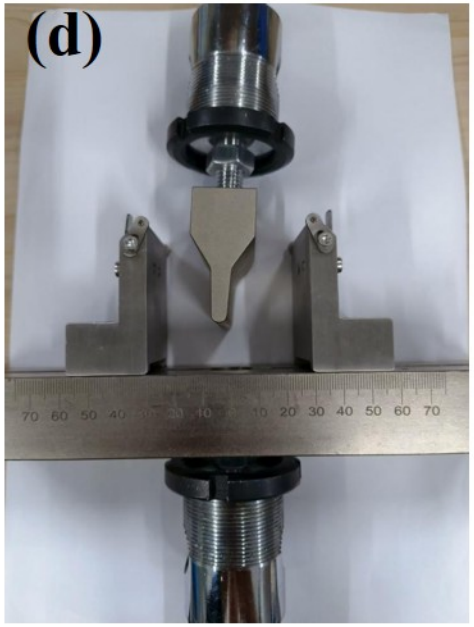
(d)
70 60 50 40 30 20 10 10 20 30 40 50 60 70

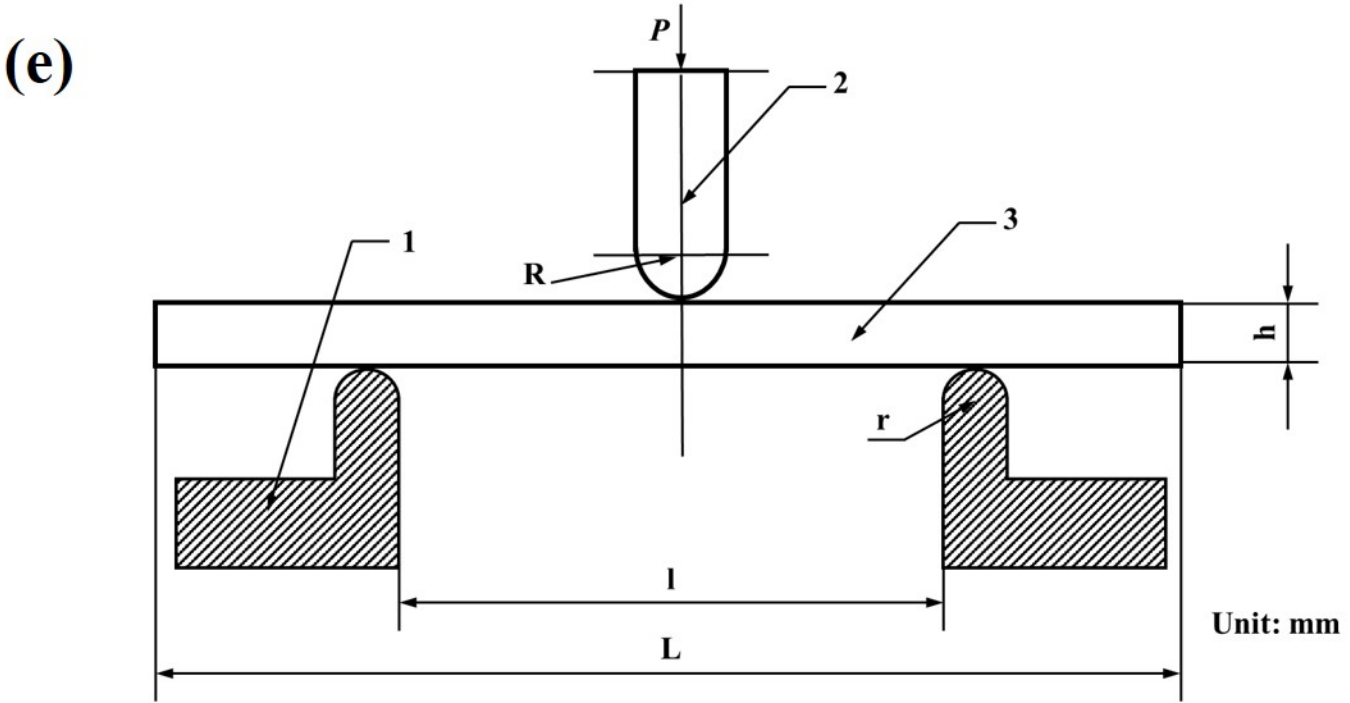
(e)
P
2
1
R
3
h
r
l
L
Unit: mm

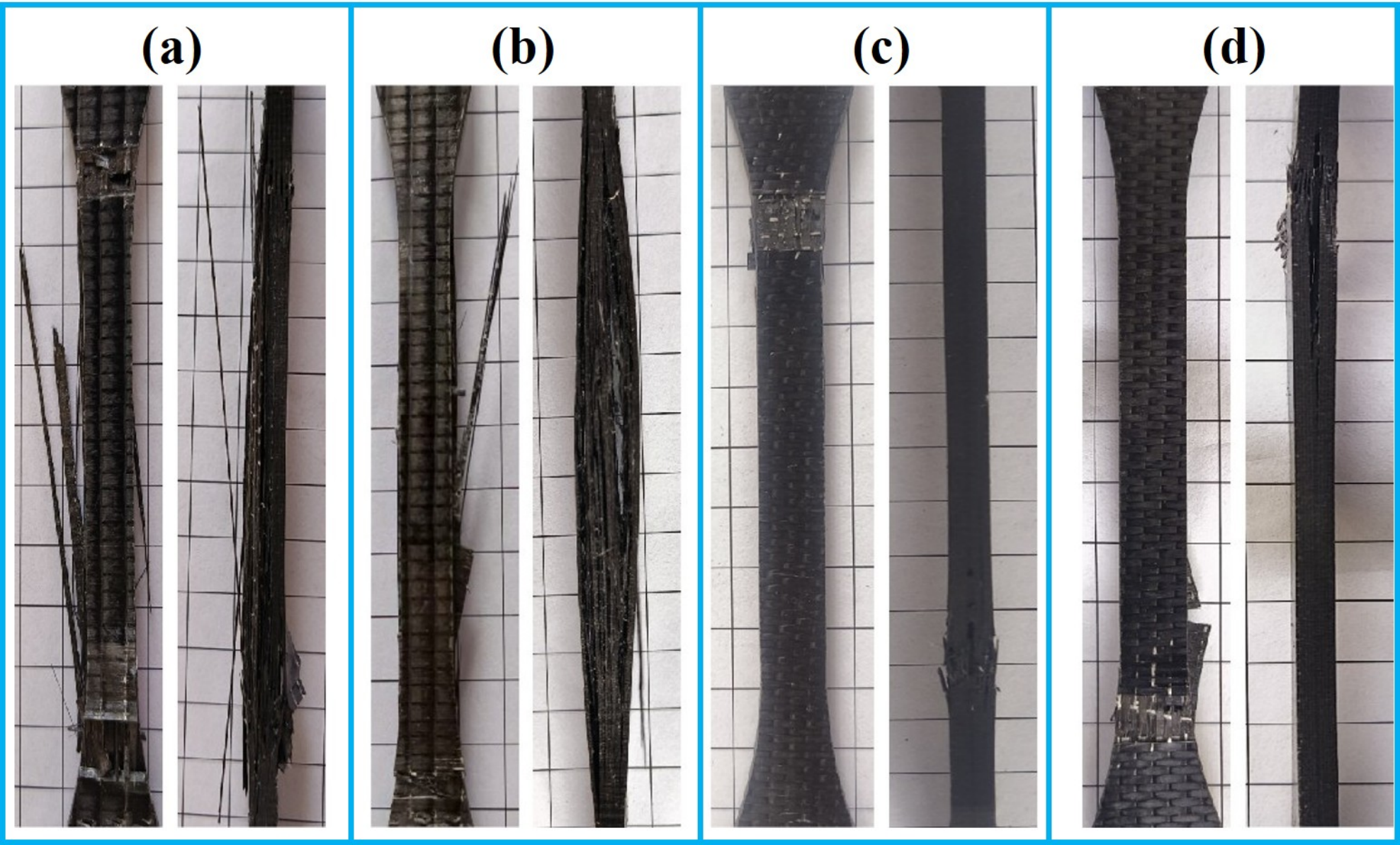
(a)
(b)
(c)
(d)

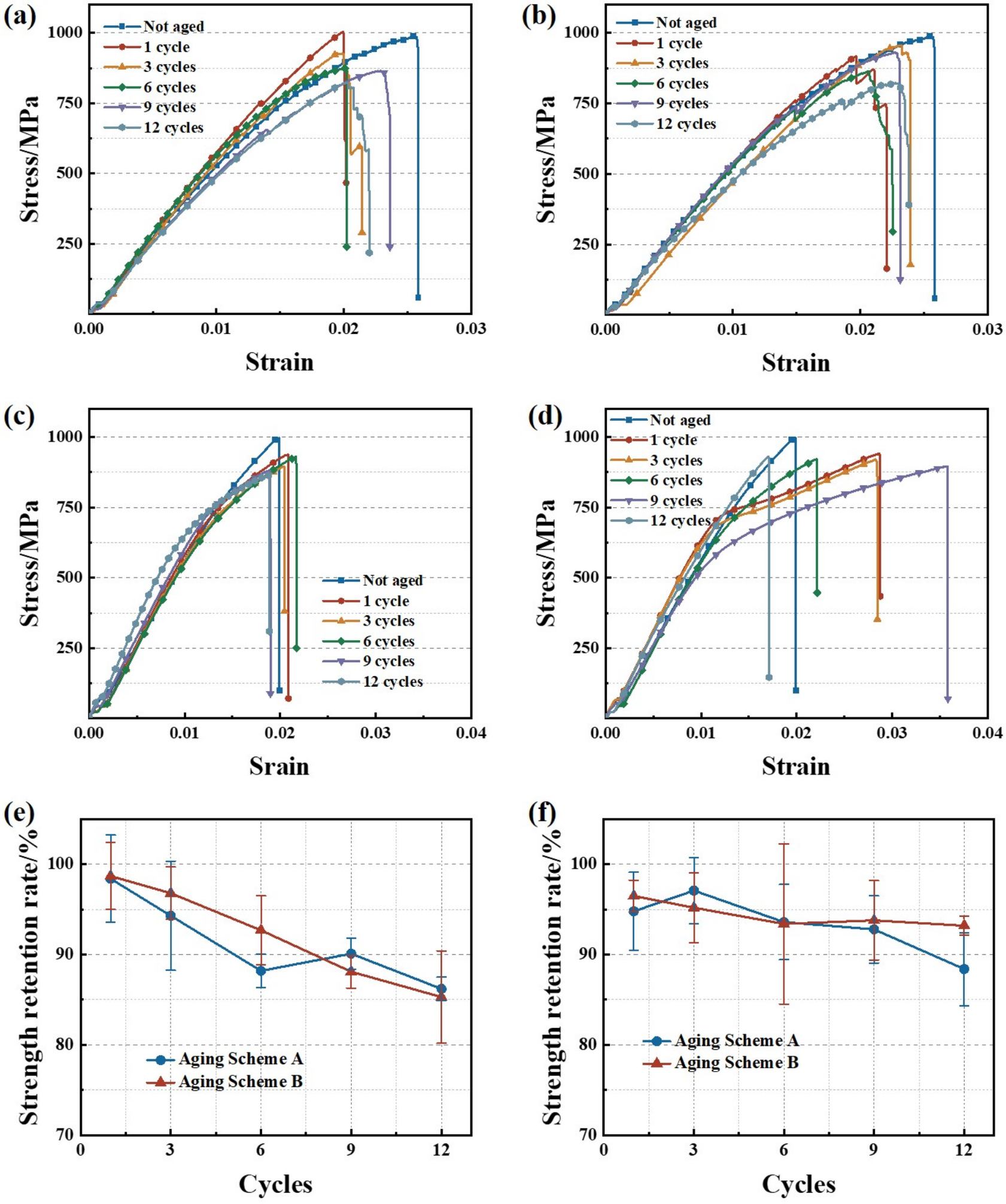
(a)
Not aged
1 cycle
3 cycles
6 cycles
9 cycles
12 cycles
Stress/MPa
Strain
(b)
Not aged
1 cycle
3 cycles
6 cycles
9 cycles
12 cycles
Stress/MPa
Strain
(c)
Not aged
1 cycle
3 cycles
6 cycles
9 cycles
12 cycles
Stress/MPa
Srain
(d)
Not aged
1 cycle
3 cycles
6 cycles
9 cycles
12 cycles
Stress/MPa
Strain
(e)
Aging Scheme A
Aging Scheme B
Strength retention rate/%
Cycles
(f)
Aging Scheme A
Aging Scheme B
Strength retention rate/%
Cycles

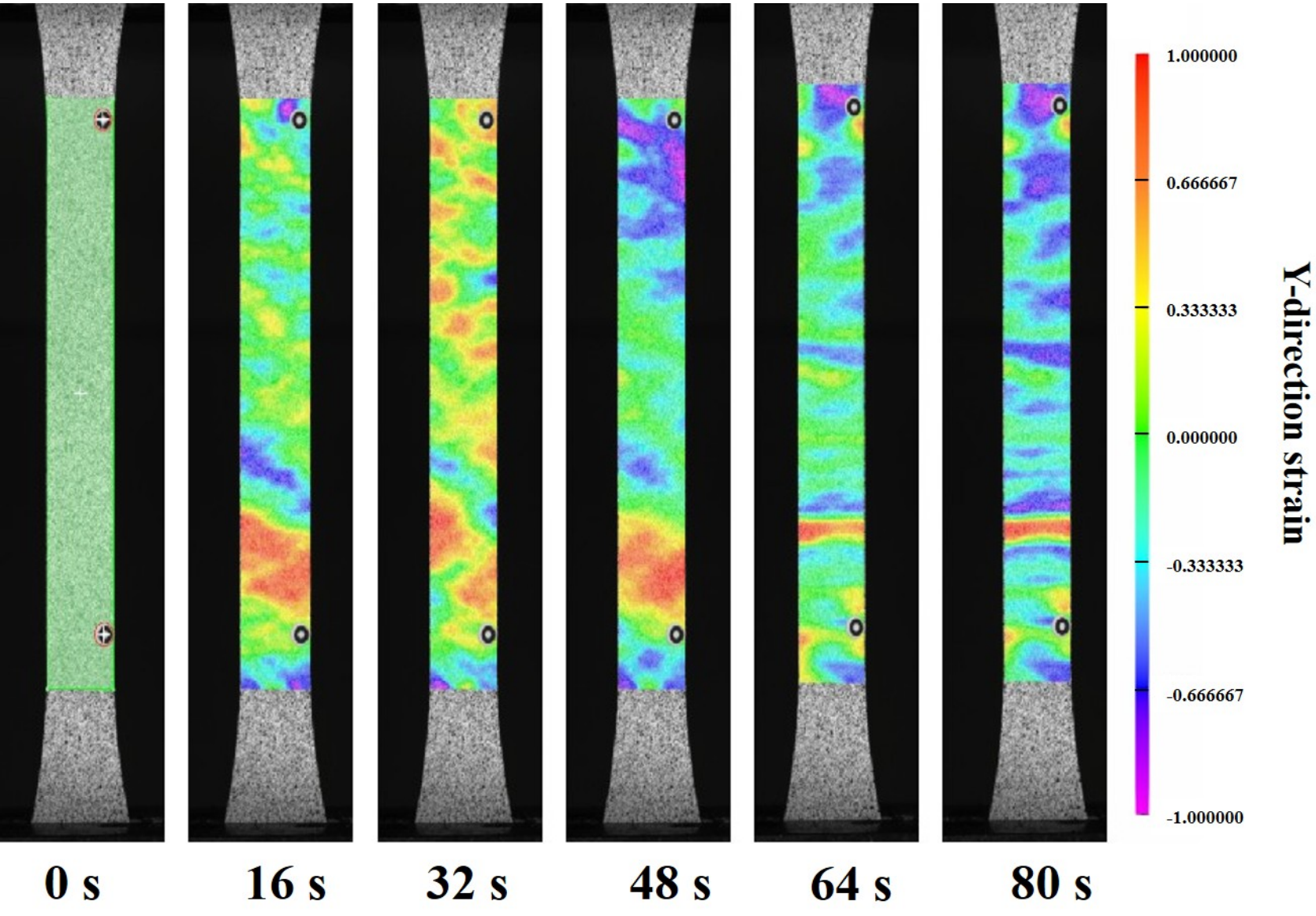
1.000000
0.666667
0.333333
0.000000
-0.333333
-0.666667
-1.000000
Y-direction strain
0 s
16 s
32 s
48 s
64 s
80 s

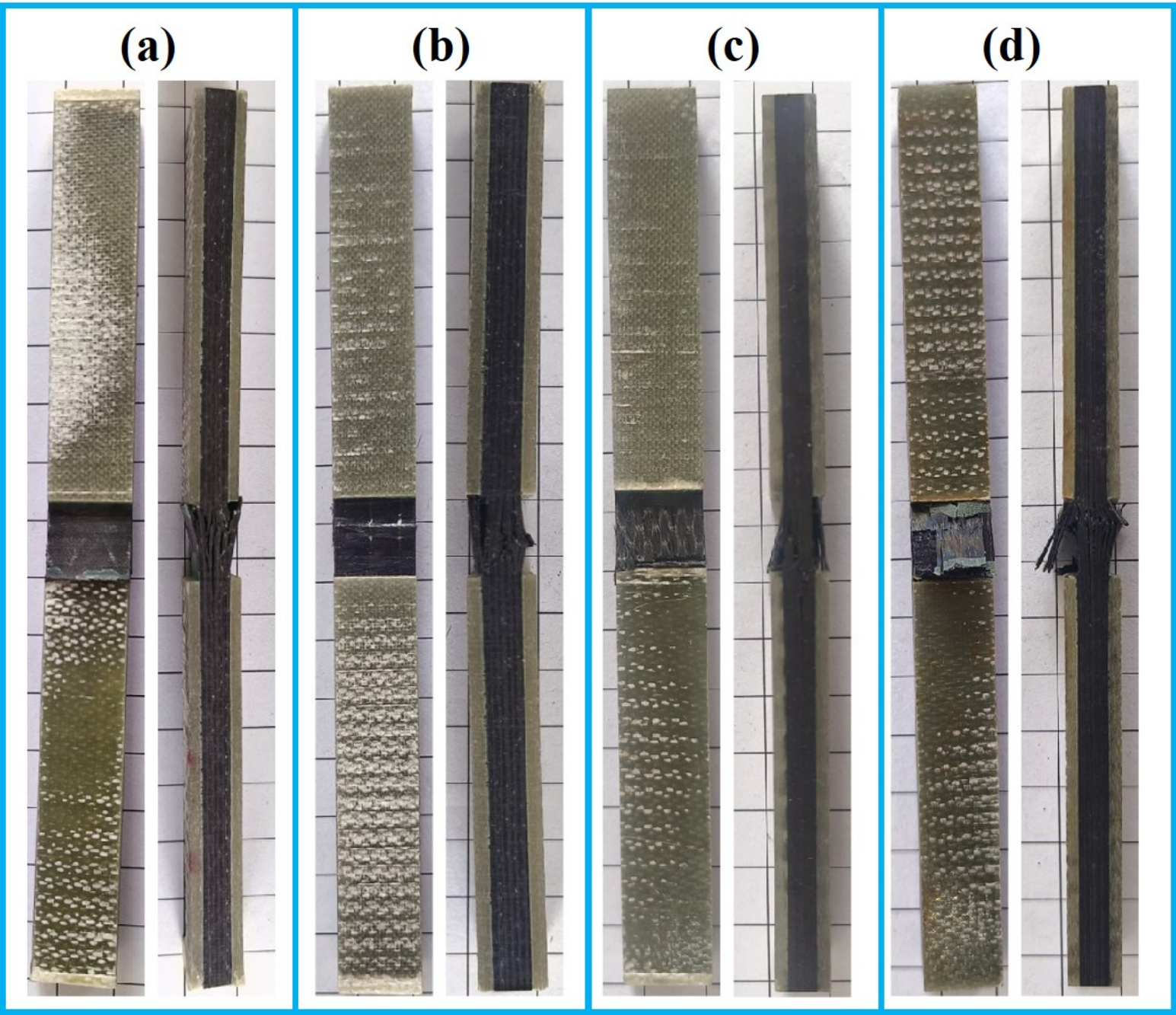
(a)
(b)
(c)
(d)

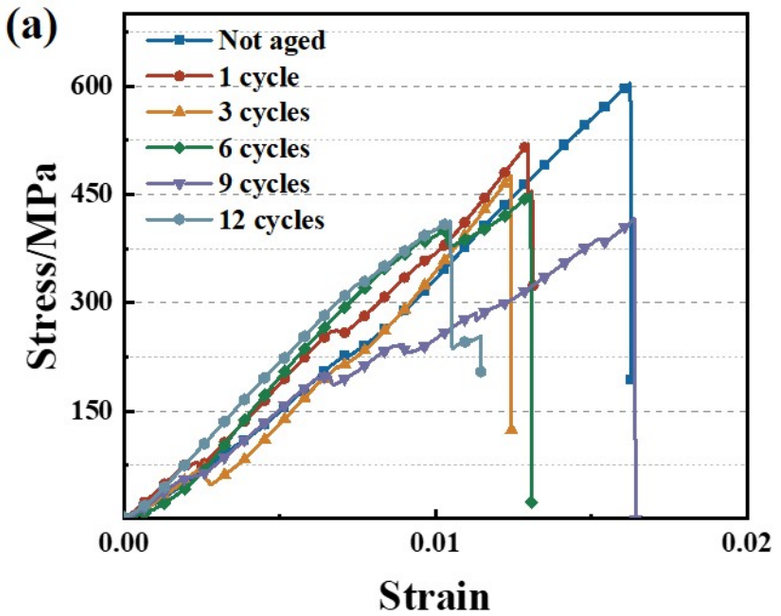
(a)
Not aged
1 cycle
3 cycles
6 cycles
9 cycles
12 cycles
Stress/MPa
600
450
300
150
0.00
0.01
0.02
Strain

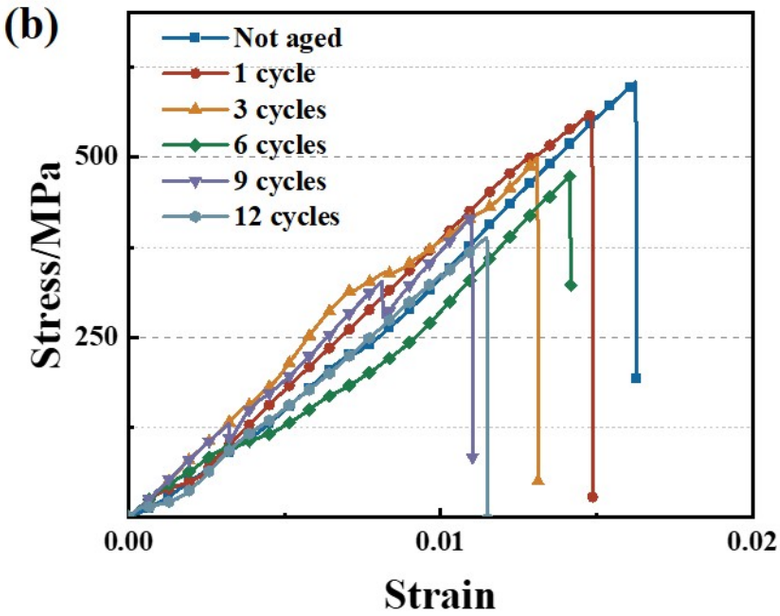
(b)
Not aged
1 cycle
3 cycles
6 cycles
9 cycles
12 cycles
Stress/MPa
500
250
0.00
0.01
0.02
Strain

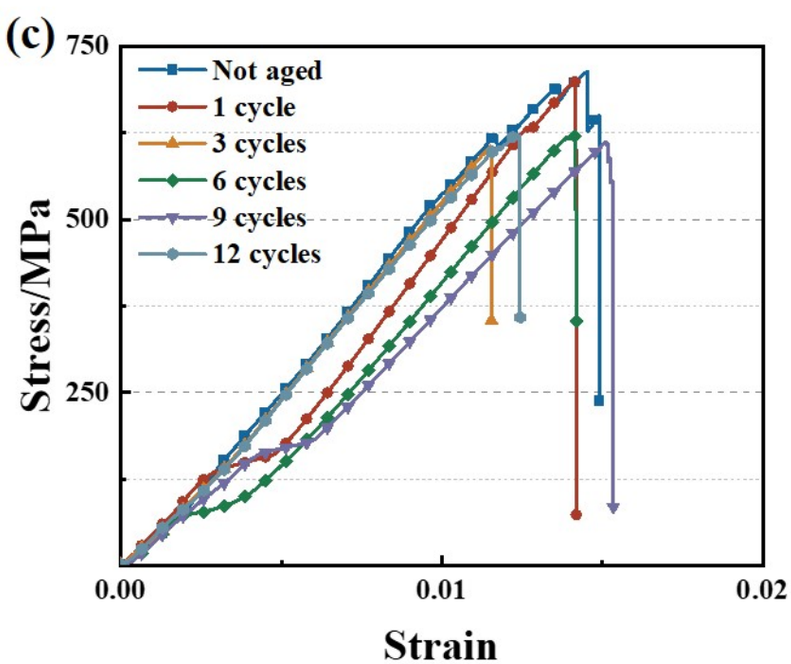
(c)
Not aged
1 cycle
3 cycles
6 cycles
9 cycles
12 cycles
Stress/MPa
750
500
250
0.00
0.01
0.02
Strain

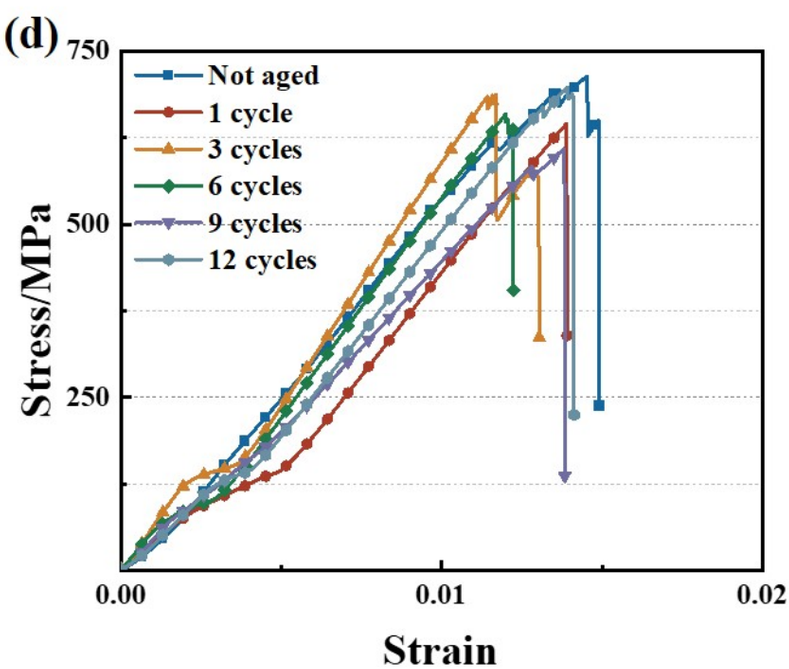
(d)
Not aged
1 cycle
3 cycles
6 cycles
9 cycles
12 cycles
Stress/MPa
750
500
250
0.00
0.01
0.02
Strain

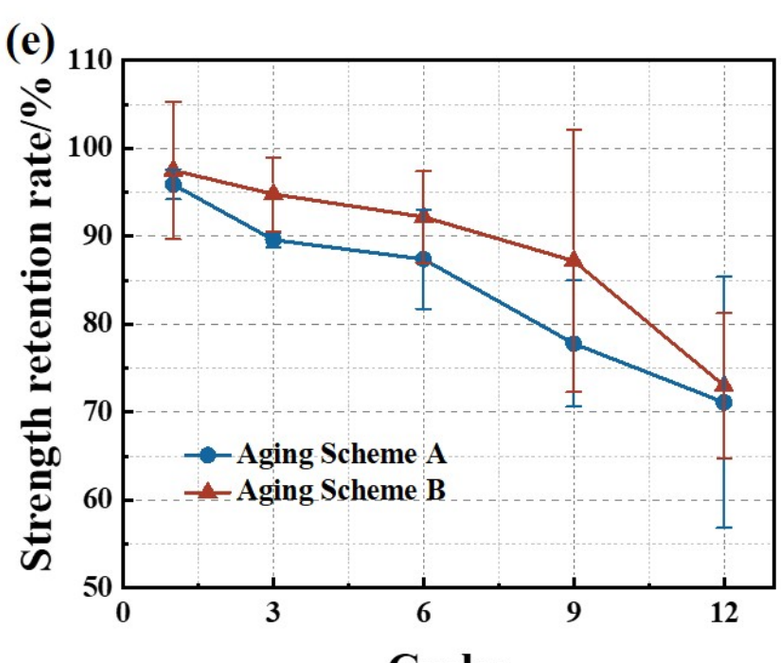
(e)
Strength retention rate/%
110
100
90
80
70
60
50
0
3
6
9
12
Cycles
Aging Scheme A
Aging Scheme B

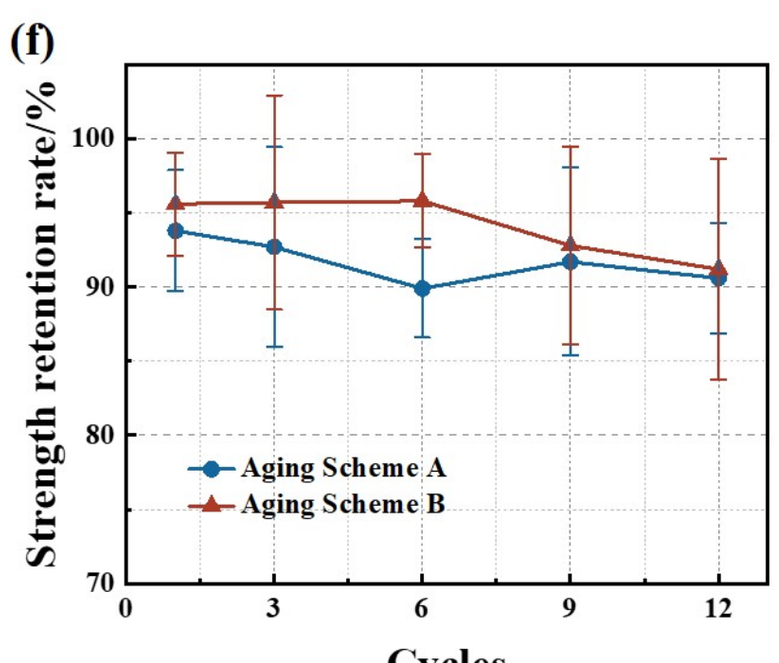
(f)
Strength retention rate/%
100
90
80
70
0
3
6
9
12
Cycles
Aging Scheme A
Aging Scheme B

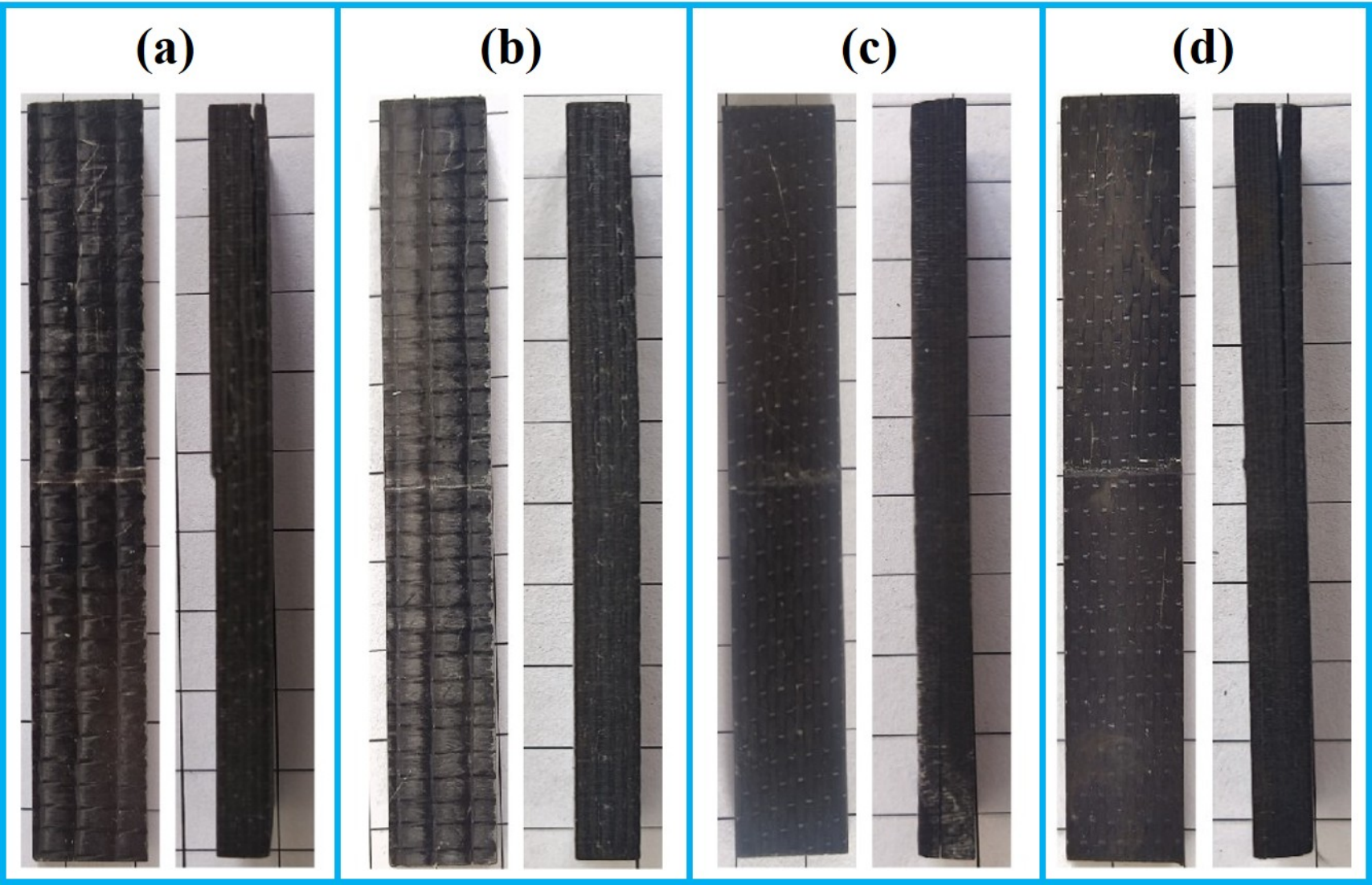
(a)
(b)
(c)
(d)